Microglial dysregulation promotes aberrant synaptic engulfment and CXCL10-associated CD8$^+$ T-cell accumulation in CMT2A mice

Shuting Zhao[#1,5], Yutong Li[#1,5], Ran Sui[2,3], Tian Xin[1], Dejun Kong[2,3], Bowen Hu[1], Yuxiao Cui[4], Yang Liu[*2,3], Guo Chen[*2,3], and Zhaowei Liu[*1,5]

1 School of Medicine, Nankai University, No. 38 Tongyan Road, Jinnan District, Tianjin 300350, China.

2 College of Life Sciences, Nankai University, No. 94 Weijin Road, Nankai District, Tianjin 300071, China.
3 State Key Laboratory of Medicinal Chemical Biology, Haihe Laboratory of Cell Ecosystem, Nankai University, No. 38 Tongyan Road, Jinnan District, Tianjin 300350, China.

4 College of Environmental Science and Engineering, Nankai University, No. 38 Tongyan Road, Jinnan District, Tianjin 300350, China.

5 Tianjin Key Laboratory of Tumor Microenvironment and Neurovascular Regulation, Nankai University, No. 38 Tongyan Road, Haihe Education Park, Tianjin, China

# These authors contributed equally to this work.

*Corresponding author:

Zhaowei Liu

School of Medicine, Nankai University, No. 38 Tongyan Road, Jinnan District, Tianjin 300350, China

Email: zhaoweiliu@nankai.edu.cn

Tel: +86-15022644561

Guo Chen

College of Life Sciences, Nankai University, No. 94 Weijin Road, Tianjin, 300071, China; State Key Laboratory of Medicinal Chemical Biology, Nankai University, No. 38 Tongyan Road, Jinnan District, Tianjin 300350, China.

Email: chenguo@nankai.edu.cn

Yang Liu

College of Life Sciences, Nankai University, Weijin Road 94#, Tianjin, 300071, China; State Key Laboratory of Medicinal Chemical Biology, Nankai University, No. 38 Tongyan Road, Jinnan District, Tianjin 300350, China.

Email: yangliu1026@nankai.edu.cn

Abstract

Charcot–Marie–Tooth disease type 2A (CMT2A), caused by pathogenic variants in MFN2, is primarily recognized as a peripheral axonopathy. Depression and psychological distress have also been reported in patients with CMT, but it remains unclear whether MFN2 mutations are associated with central neuroimmune alterations that contribute to behavioral changes. We compared Mfn2 T105M and R94W mouse models and observed anxiety-, repetitive-, and depression-related behavioral abnormalities. To assess the contribution of basolateral amygdala (BLA) microglia, we used CX3CR1-directed, Cre-dependent designer receptors exclusively activated by designer drugs (DREADDs). Chemogenetic Gi activation, but not Gq activation, improved behavioral outcomes in R94W mice.

R94W microglia showed increased somatic volume and surface area, increased COX IV immunoreactivity, and more synaptophysin- and PSD95-positive cargo. Bulk BLA synaptophysin levels were unchanged, suggesting enhanced spatially restricted microglial phagocytosis without evidence of widespread synaptic protein loss. Bulk RNA sequencing of the BLA identified phagosome, innate immune, antigen-processing and presentation, chemokine-signaling, and T-cell-related programs, many of which were attenuated by microglial Gi-DREADD activation. The R94W BLA also showed increased MYD88, NF-κB p65, and CXCL10 signals, accompanied by marked $CD8^+$ T-cell accumulation. Gi-DREADD activation reduced these inflammatory signals, microglial morphological changes, synaptic cargo, and $CD8^+$ T-cell accumulation. AMG487 treatment reduced marble burying, BLA $CD8^+$ T-cell accumulation, and microglial CXCL10 signal, and partially improved elevated-plus-maze measures.

These results suggest that BLA microglial dysregulation contributes to behavioral abnormalities associated with MFN2 R94W and is accompanied by abnormal synaptic engulfment, CXCL10-associated $CD8^+$ T-cell accumulation, and inflammatory changes. They also extend the pathophysiological framework of CMT2A beyond peripheral axons and suggest a neuroimmune component to the neurobehavioral burden reported in CMT.

Keywords: CMT2A; *Mfn2*; microglia; synaptic engulfment; CXCL10

Introduction

Charcot–Marie–Tooth disease type 2A (CMT2A) is an inherited axonal neuropathy caused by pathogenic variants in MFN2, which encodes the mitochondrial outer-membrane GTPase mitofusin 2 [1]. MFN2 coordinates mitochondrial fusion and contributes to mitochondrial transport, organelle contacts, and cellular metabolic adaptation. Pathogenic *Mfn2* variants can therefore disrupt multiple mitochondrial processes that are particularly important for the maintenance of long peripheral axons, contributing to the axonal degeneration characteristic of CMT2A[2-4]. Accordingly, most mechanistic studies have focused on peripheral nerves and motor neurons, whereas the consequences of MFN2 dysfunction in the central nervous system (CNS) remain less well defined.

Importantly, CMT may involve neurobehavioral manifestations beyond peripheral motor and sensory deficits, with depression and psychological distress reported in patients [5]. Experimental evidence further suggests that MFN2 in the brain can influence behavioral regulation: reduced *Mfn2* expression in the nucleus accumbens was associated with anxiety- and depression-like behaviors, whereas local MFN2 overexpression reversed these phenotypes [6]. Cell-type-specific manipulation of accumbal *Mfn2* also altered anxiety-related and social dominance behaviors [7]. Together, these findings raise the possibility that disease-associated MFN2 variants influence behavior through central mechanisms in addition to their established effects on peripheral axons.

Microglia are highly plastic CNS-resident myeloid cells that regulate neural-circuit homeostasis through surveillance, inflammatory signaling, and phagocytosis. During development, microglia refine neural circuits by engulfing synaptic material[8, 9]; in disease, excessive or mistargeted engulfment can contribute to circuit dysfunction. Because microglial activity is highly sensitive to metabolic and mitochondrial perturbations, MFN2 dysfunction could alter microglial state even in the absence of widespread neuronal degeneration [10]. Whether microglia contribute to behavioral abnormalities associated with *Mfn2* mutations remains unknown.

Microglia also bridge innate and adaptive immunity. MYD88-dependent signaling downstream of Toll-like and interleukin-1 receptors activates NF-κB and induces inflammatory cytokines and chemokines [11]. Among these, CXCL10 can promote the accumulation of CXCR3-expressing immune cells in the CNS. Activated microglia have been shown to facilitate T-cell infiltration and neurodegeneration in tauopathy [12], while recent work in aging-associated white-matter degeneration further demonstrated that maladaptive microglial activation drives CXCL10-dependent accumulation of pathogenic $CD8^+$ T cells [13]. Whether a comparable microglia-associated inflammatory response occurs in a genetic axonal neuropathy has not been established.

Our previous work showed that chemogenetic modulation of BLA microglia alleviated sleep deprivation-induced behavioral deficits and associated inflammatory, synaptic, and mitochondrial abnormalities [14], suggesting a broader role for BLA microglia in socio-emotional dysfunction.

Here, we used complementary chemogenetic strategies to examine BLA microglia in Mfn2 R94W mice. Behavioral, imaging, molecular, and transcriptomic analyses indicated increased microglial synaptic engulfment and were accompanied by enhanced MYD88–NF-κB signaling, CXCL10 expression, and $CD8^+$ T-cell accumulation. Gi-DREADD activation attenuated these abnormalities and improved behavioral outcomes.

Results

Mfn2 T105M and R94W mice exhibit overlapping but distinct behavioral abnormalities

We first compared repetitive-, depression-, and anxiety-related behavioral phenotypes among wild-type (WT), *Mfn2* T105M, and *Mfn2* R94W mice (Fig. 1a). In the marble-burying test, both T105M and R94W mice buried significantly more marbles than WT controls (one-way ANOVA, $F(2,22) = 12.79$, $P = 0.0002$; T105M, $P < 0.001$; R94W, $P < 0.01$; Fig. 1b), indicating increased marble-burying behavior. Grooming bouts also differed among groups ($F(2,22) = 5.495$, $P = 0.0116$); the increase was significant in T105M mice ($P < 0.01$), whereas the increase in R94W mice did not reach significance (Fig. 1c). Both mutant groups exhibited increased immobility in the tail-suspension test ($F(2,22) = 24.18$, $P < 0.0001$; both $P < 0.001$ versus WT; Fig. 1d), consistent with a depression-related behavioral phenotype.

Representative movement trajectories in the elevated plus maze showed reduced exploration of the open arms by both mutant groups (Fig. 1e). T105M and R94W mice spent less time in the open arms ($F(2,26) = 7.002$, $P = 0.0037$; T105M, $P < 0.05$; R94W, $P < 0.01$) and more time in the closed arms ($F(2,26) = 8.212$, $P = 0.0017$; T105M, $P < 0.05$; R94W, $P < 0.01$) than WT mice. R94W mice also made fewer open-arm entries ($F(2,26) = 4.869$, $P = 0.0160$; $P < 0.05$), whereas closed-arm entries did not differ among groups ($F(2,26) = 1.428$, $P = 0.2580$). The open-arm-to-closed-arm duration ratio was reduced in both T105M and R94W mice ($F(2,26) = 7.572$, $P = 0.0026$; $P < 0.05$ and $P < 0.01$, respectively), whereas the corresponding entry ratio was unchanged (Fig. 1f).

The two *Mfn2* variants produced overlapping, but distinct, behavioral phenotypes. Both were associated with increased marble burying and tail-suspension immobility, as well as reduced open-arm exploration. Increased grooming was more evident in T105M mice, whereas reduced open-arm entries were observed only in R94W

mice. Because R94W mice showed a robust behavioral phenotype and Arg94 is a recurrent mutational hotspot in *Mfn2*, with both R94W and R94Q repeatedly identified in CMT2A, we selected the R94W model for subsequent mechanistic experiments [1, 15].

Chemogenetic Gi activation in BLA CX3CR1-targeted cells ameliorates behavioral abnormalities in R94W mice

To investigate whether CX3CR1-expressing cells in the BLA contribute to the behavioral abnormalities of R94W mice, we bilaterally co-injected AAV2/9-Cx3cr1-Cre-3 ×FLAG with the Cre-dependent AAV2/9-CAG-DIO-hM4D(Gi)-mCherry or AAV2/9-CAG-DIO-hM3D(Gq)-mCherry vector into the BLA of WT and R94W mice (Fig. 2a). Histological examination confirmed mCherry expression within the BLA. mCherry showed limited colocalization with NeuN-positive neurons and GFAP-positive astrocytes, supporting minimal neuronal and astrocytic off-target expression (Fig. 2b,c). Three weeks after viral injection, behavioral testing was performed 30 min after CNO administration (Fig. 2d).

In the open-field test, representative movement trajectories suggested reduced center exploration in vehicle-treated R94W mice (Fig. 2e). For center-area duration, two-way ANOVA revealed a significant genotype × treatment interaction ($F(2,59) = 3.172$, $P = 0.0492$) and a significant main effect of genotype ($F(1,59) = 8.860$, $P = 0.0042$). Post hoc comparisons showed that vehicle-treated R94W mice spent significantly less time in the center area than vehicle-treated WT mice ($P < 0.01$). This genotype-dependent difference was no longer detected under the Gi-DREADD condition, consistent with attenuation of the R94W phenotype. In contrast, R94W mice continued to show reduced center-area duration relative to the corresponding WT group following Gq-DREADD activation ($P < 0.05$). For distance travelled in the center area, two-way ANOVA revealed a significant main effect of genotype ($F(1,59) = 4.257$, $P = 0.0435$), but no significant main effect of chemogenetic treatment or genotype ×treatment interaction. This pattern suggests that Gi-DREADD activation selectively enhanced center-directed exploration in R94W mice without producing a generalized increase in locomotor activity, whereas Gq-DREADD activation did not provide a comparable behavioral benefit.

In the elevated plus maze, two-way ANOVA revealed significant main effects of genotype on closed-arm duration ($F(1,59) = 9.427$, $P = 0.0032$), open-arm entries ($F(1,59) = 6.603$, $P = 0.0127$), open-arm duration ($F(1,59) = 13.12$, $P = 0.0006$), the open-arm-to-closed-arm duration ratio ($F(1,59) = 10.22$, $P = 0.0022$), and the open-arm-to-closed-arm entry ratio ($F(1,59) = 8.685$, $P = 0.0046$). No significant genotype effect was detected for closed-arm entries.

Post hoc comparisons showed that, under the vehicle condition, R94W mice spent more time in the closed arms ($P < 0.01$), spent less time in the open arms ($P < 0.01$), and exhibited lower open-arm-to-closed-arm duration and entry ratios (both $P < 0.05$) than WT controls. These genotype-dependent differences were no longer detected under the Gi-DREADD condition, consistent with attenuation of the R94W elevated-plus-maze phenotype.

Gi-DREADD activation shifted several elevated-plus-maze measures toward control values, including closed-arm duration, open-arm duration, and the open-arm-to-closed-arm duration and entry ratios. Gq-DREADD activation did not yield a comparable pattern: the open-arm-to-closed-arm duration ratio remained lower in R94W mice than in the corresponding WT group ($P < 0.05$). Thus, Gi activation in BLA CX3CR1-targeted cells improved anxiety-related behavior without uniformly increasing locomotion. Because Gi-DREADD activation produced consistent behavioral improvements, whereas Gq-DREADD activation did not, the Gi strategy was carried forward for cellular and mechanistic analyses. R94W microglia exhibit increased COX IV immunoreactivity and synaptic cargo that are attenuated by Gi-DREADD activation

Before examining cell-resolved microglial phenotypes, we assessed the regional distribution of major neuronal and glial markers in WT and R94W brains. NeuN immunostaining showed broadly preserved neuronal regional distribution, whereas GFAP immunoreactivity appeared increased in the R94W hippocampus, suggesting an accompanying astrocytic response (Supplementary Fig. 2a,b). Quantitative analysis further revealed a significant increase in the Iba1-positive area within the R94W BLA compared with WT controls ($P < 0.001$; Supplementary Fig. 2c), supporting a prominent microglial response in this region. Analysis of the Allen Brain Cell Atlas showed that *Aif1* expression was selectively enriched in microglia, enabling identification of the microglial population. Among the major CNS cell types examined, microglia exhibited the highest relative *Mfn2* expression signal, exceeding that observed in neurons and astrocytes (Supplementary Fig. 2d,e). Although *Mfn2* was broadly expressed across CNS cell populations, its relative enrichment in microglia suggests that microglial function may be particularly susceptible to disruption by MFN2 mutations.

We next examined mitochondrial respiratory-chain proteins and synaptic markers in the BLA. Western blot analysis showed no significant differences in the bulk abundance of mitochondrial respiratory-chain complexes I, II, III, and V among the experimental groups (Fig. 3a,b). Similarly, total BLA synaptophysin (SYP) abundance was not significantly altered by genotype or chemogenetic treatment (Fig. 3c). These results indicated that R94W mice did not exhibit a uniform change in the examined mitochondrial respiratory-chain proteins or global SYP abundance at the whole-tissue level.

In contrast, cell-resolved immunofluorescence revealed significant group differences in COX IV immunoreactivity within mCherry-positive microglia (one-way ANOVA, $F(2,6) = 75.42$, $P < 0.0001$; Fig. 3d,g). Post hoc comparisons showed that microglial COX IV immunoreactivity was significantly higher in R94W mice than in WT controls ($P < 0.001$) and was significantly reduced by Gi-DREADD activation in R94W mice ($P < 0.01$). Although the COX IV signal remained numerically above the control level following Gi-DREADD activation, this difference was not statistically significant. These findings indicate a cell-associated alteration in COX IV immunoreactivity that was not evident from the bulk respiratory-chain protein analysis.

Quantification of internalized SYP-positive material revealed a significant overall group difference (one-way ANOVA, $F(2,6) = 118.0$, $P < 0.0001$; Fig. 3e,h). R94W microglia contained a larger area of SYP-positive puncta within mCherry-positive regions than WT microglia ($P < 0.0001$), consistent with increased uptake of presynaptic material. Gi-DREADD activation reduced the internalized SYP-positive area in R94W microglia ($P < 0.01$), indicating attenuation of the enhanced synaptic-cargo phenotype. The absence of a corresponding reduction in total BLA SYP abundance suggests a spatially restricted increase in microglial synaptic cargo rather than widespread loss of presynaptic protein.

These experiments define a cell-resolved R94W microglial phenotype in which increased COX IV immunoreactivity accompanies greater accumulation of synaptic material. Both features were attenuated by Gi-DREADD activation, despite the limited changes detected in bulk BLA protein abundance (Fig. 3f).

Gi-DREADD activation ameliorates behavioral abnormalities in *Cx3cr1*-Cre/R94W mice

To further evaluate the contribution of BLA microglia to the R94W behavioral phenotype, we crossed *Cx3cr1*-Cre mice with *Mfn2* R94W mice and bilaterally injected the Cre-dependent AAV2/9-CAG-DIO-hM4D(Gi)-mCherry vector into the BLA (Fig. 4a,b). Behavioral testing was conducted three weeks after viral injection, 30 min after vehicle or CNO administration.

In the elevated-plus-maze test, significant group differences were observed in open-arm duration ($F(2,25) = 7.708$, $P = 0.0025$; Fig. 4c). R94W+Veh mice spent less time in the open arms than Ctrl+Veh mice ($P < 0.01$), whereas Gi-DREADD activation increased open-arm duration relative to vehicle-treated R94W mice ($P <$

0.05). Closed-arm duration also differed among groups (F(2, 25) = 6.674, $P = 0.0048$), with R94W+Veh mice spending more time in the closed arms than Ctrl+Veh mice ($P < 0.01$); the reduction following Gi-DREADD activation did not reach statistical significance. No significant group difference was detected in the proportion of open-arm entries (F(2, 25) = 2.242, $P = 0.1271$). In contrast, the proportion of time spent in the open arms differed significantly among groups (F(2, 25) = 7.831, $P = 0.0023$): it was reduced in R94W+Veh mice compared with Ctrl+Veh mice ($P < 0.01$) and increased following Gi-DREADD activation ($P < 0.05$).

The proportion of open-arm entries relative to total arm entries differed significantly among the groups ($F(2,39) = 4.405$, $P = 0.0188$). This ratio was significantly reduced in vehicle-treated R94W mice compared with control mice ($P < 0.05$) and was significantly increased by Gi-DREADD activation ($P < 0.05$). The proportion of time spent in the open arms relative to total arm time also showed a significant group effect ($F(2,39) = 6.334$, $P = 0.0041$). Vehicle-treated R94W mice exhibited a markedly lower open-arm duration ratio than control mice ($P < 0.01$), whereas Gi-DREADD activation produced a numerical shift toward control values without reaching statistical significance.

Marble-burying behavior also differed significantly among the groups (one-way ANOVA, $F(2,25) = 14.69$, $P < 0.0001$; Fig. 4d). Vehicle-treated R94W mice buried significantly more marbles than control mice ($P < 0.001$), and Gi-DREADD activation significantly reduced marble burying in R94W mice ($P < 0.001$).

Functional enrichment analysis of the BLA RNA-sequencing dataset presented in Figure 5 was consistent with the behavioral findings. Genes altered after Gi-DREADD activation were associated with behavioral regulation, circadian rhythm and sleep, neurotransmitter signaling, cognition, and locomotor behavior (adjusted $P < 0.05$; Fig. 4e). The most reproducible behavioral effects of Gi activation were improved open-arm exploration and reduced marble burying.

BLA transcriptomics reveals phagocytic and neuroimmune programs in R94W mice that are broadly attenuated by Gi-DREADD activation

Principal-component analysis showed partial separation of the three experimental groups, supporting distinct BLA transcriptional profiles associated with the R94W genotype and Gi-DREADD intervention (Supplementary Fig. 8a).

To characterize the molecular changes associated with the R94W phenotype and its response to microglial Gi-DREADD activation, we performed bulk RNA sequencing of BLA tissue from Ctrl+Veh, R94W+Veh, and R94W+CNO mice (Fig. 5a). Comparison of R94W+Veh with Ctrl+Veh identified 897 differentially expressed genes, including 482 upregulated and 415 downregulated genes (Fig. 5c). Comparison of R94W+CNO with R94W+Veh identified 754 differentially expressed genes, of which 385 were upregulated and 369 were downregulated following Gi-DREADD activation (Fig. 5d). Venn analysis demonstrated partially overlapping gene sets among the three pairwise comparisons, indicating both R94W-associated transcriptional changes and a substantial response to Gi-DREADD activation (Fig. 5b).

Gene Ontology analysis of genes upregulated in R94W+Veh mice revealed enrichment of immune effector processes, responses to interferon-γ and other biotic stimuli, leukocyte cell–cell adhesion, adaptive and lymphocyte-mediated immunity, cell killing, MHC protein complexes, and phagocytic-vesicle-related cellular components (Fig. 5e). Molecular-function terms related to chemokine and cytokine activity, cytokine-receptor binding, GTPase activity, and MHC protein binding were also enriched. These findings indicate coordinated activation of innate and adaptive immune, antigen-presentation, and phagocytic programs in the R94W BLA.

Conversely, genes downregulated in R94W+CNO mice relative to R94W+Veh mice were enriched in many of the same functional categories, including interferon responses, regulation of immune effector processes, lymphocyte-mediated immunity, cell killing, MHC protein complexes, and phagocytic-vesicle and

phagosome-related components (Fig. 5f). This reciprocal pathway-level pattern suggests that microglial Gi-DREADD activation consistently attenuated the neuroimmune and phagocytic transcriptional state associated with the R94W genotype.

KEGG enrichment analysis further showed that genes upregulated in R94W+Veh mice were associated with NOD-like receptor and Toll-like receptor signaling, antigen processing and presentation, cytokine–cytokine receptor interactions, chemokine signaling, phagosomes, T-cell receptor signaling, T helper-cell differentiation, TNF signaling, natural-killer-cell-mediated cytotoxicity, and PD-1/PD-L1 checkpoint signaling (Fig. 5g). Many of these pathways, including antigen processing and presentation, NOD-like receptor signaling, chemokine signaling, T-cell receptor signaling, TNF signaling, phagosomes, and natural-killer-cell-mediated cytotoxicity, were enriched among genes downregulated following Gi-DREADD activation (Fig. 5h). Complementary GO analysis showed that genes downregulated in R94W+Veh mice were enriched in ion-transport, muscle-contraction, synaptic, axonal, and neuronal-compartment-related terms (Supplementary Fig. 4a). Conversely, genes upregulated following Gi-DREADD activation were enriched in neuropeptide signaling, neurotransmitter loading into synaptic vesicles, ion and organic-compound transport, and neuronal or axonal compartments, suggesting re-engagement of neuronal signaling and transport-related transcriptional programs (Supplementary Fig. 4b).

The transcriptomic profile therefore points to coordinated activation of phagocytic, innate immune, antigen-presentation, chemokine, and lymphocyte-related programs in the R94W BLA. Gi-DREADD activation broadly attenuated these pathway-level changes, rather than affecting only a small number of isolated genes.

Gi-DREADD activation attenuates microglial reactivity, morphological enlargement, and synaptic engulfment in R94W mice

We first examined the abundance of microglial and astrocytic markers in the BLA. One-way ANOVA revealed significant group differences in Iba1 protein abundance ($F(2,6) = 6.719$, $P = 0.0294$; Supplementary Fig. 3a,b). Post hoc comparisons showed that Iba1 abundance was significantly increased in R94W+Veh mice compared with Ctrl+Veh mice ($P < 0.05$) and was reduced following Gi-DREADD activation ($P < 0.05$). GFAP protein abundance also differed significantly among the groups ($F(2,6) = 17.08$, $P = 0.0033$). GFAP abundance was reduced in R94W+Veh mice relative to Ctrl+Veh mice ($P < 0.05$) and increased following Gi-DREADD activation ($P < 0.01$). These findings indicate that the R94W genotype and microglial Gi-DREADD activation were accompanied by distinct changes in microglial and astrocytic marker abundance in the BLA.

In the same genetic-cross cohort, bulk BLA SYP abundance remained unchanged among Ctrl+Veh, R94W+Veh, and R94W+CNO mice (Supplementary Fig. 5a). Synapse-related GO cellular-component terms showed no evidence of broad depletion in R94W mice, supporting a spatially restricted increase in microglial synaptic cargo rather than widespread loss of synaptic proteins (Supplementary Fig. 5b). The heatmap of mitochondrial function-related differentially expressed genes identified in the R94W BLA showed a mixture of upregulated and downregulated transcripts. Whole-BLA Western blotting revealed reduced COX IV abundance in R94W mice that was not significantly restored by Gi-DREADD activation. In contrast, cell-resolved imaging showed increased COX IV immunoreactivity within mCherry-positive R94W microglia, which was attenuated following Gi-DREADD activation (Supplementary Fig. 5c–e).

Consistent with the increase in Iba1 abundance, three-dimensional reconstruction revealed significant group differences in microglial volume (one-way ANOVA, $F(2,6) = 13.4$, $P = 0.0061$) and surface area ($F(2,6) = 8.988$, $P = 0.0157$; Fig. 6a,b). Post hoc comparisons showed that both microglial volume and surface area were significantly increased in R94W+Veh mice compared with Ctrl+Veh mice (both $P < 0.05$) and were significantly reduced following Gi-DREADD activation (both $P < 0.05$). In contrast, the surface-area-to-

volume ratio did not differ significantly among the groups ($F(2,6) = 0.3412$, $P = 0.7239$), suggesting proportional enlargement rather than a disproportionate alteration in surface complexity.

Gene-set enrichment analysis demonstrated positive enrichment of leukocyte-mediated immunity and phagocytic-vesicle gene sets in R94W+Veh mice relative to Ctrl+Veh mice (Fig. 6c). Both gene sets showed negative enrichment in R94W+CNO mice relative to R94W+Veh mice, consistent with suppression of immune and phagocytic transcriptional programs following Gi-DREADD activation.

Quantification of SYP-positive puncta within mCherry-positive microglia revealed a significant overall group difference (one-way ANOVA, $F(2,6) = 161.9$, $P < 0.0001$; Fig. 6d,e). R94W+Veh microglia contained significantly more SYP-positive puncta than Ctrl+Veh microglia ($P < 0.001$), whereas Gi-DREADD activation significantly reduced the number of microglial SYP-positive puncta in R94W mice ($P < 0.001$). PSD95-positive puncta also differed significantly among the groups ($F(2,6) = 38.19$, $P = 0.0004$). The number of PSD95-positive puncta within mCherry-positive microglia was markedly increased in R94W+Veh mice compared with Ctrl+Veh mice ($P < 0.001$) and was significantly reduced following Gi-DREADD activation ($P < 0.01$). Three-dimensional reconstructions confirmed the localization of SYP- and PSD95-positive puncta within mCherry-positive microglial volumes, with fewer synaptic puncta observed following Gi-DREADD activation, consistent with the quantitative analysis (Fig. 6f). Representative rotational renderings further visualized PSD95-positive cargo within mCherry-positive microglial volumes in an R94W+Veh mouse (Supplementary Video 1) and an R94W+CNO mouse (Supplementary Video 2), illustrating the reduced microglia-associated PSD95 signal following Gi-DREADD activation.

Taken together, the R94W BLA showed increased Iba1 abundance, increased microglial volume and surface area with a preserved surface-area-to-volume ratio, enrichment of immune and phagocytic programs, and greater microglial accumulation of both presynaptic and postsynaptic material. The consistent attenuation of these changes after Gi-DREADD activation is consistent with the suppression of an altered microglial phagocytic state.

Increased microglial CXCL10 expression is associated with $CD8^+$ cell accumulation in the R94W BLA

Based on the enrichment of chemokine, antigen-presentation, and lymphocyte-related pathways, we next investigated a potential microglia-associated CXCL10–$CD8^+$ cell response in the R94W BLA (Fig. 7a). Heatmap analysis of the BLA bulk RNA-sequencing data showed coordinated upregulation of differentially expressed genes involved in antigen presentation and chemokine signaling, including *Cxcl10*, *Cxcl9*, *Ccl5*, and MHC-associated genes, in R94W+Veh mice (Fig. 7b). Genes related to $CD8^+$ T-cell activation and cytotoxic function were also increased. Gi-DREADD activation shifted many of these transcripts toward the control expression profile, indicating attenuation of both chemokine/antigen-presentation and T-cell-related transcriptional programs.

Cell-resolved immunofluorescence revealed significant group differences in CXCL10 intensity within mCherry-positive microglia (one-way ANOVA, $F(2,6) = 111.2$, $P < 0.0001$; Fig. 7c,e). Microglial CXCL10 intensity was markedly increased in R94W+Veh mice compared with Ctrl+Veh mice ($P < 0.001$) and was reduced following Gi-DREADD activation ($P < 0.001$). These findings localized the R94W-associated increase in CXCL10 signal, at least in part, to mCherry-positive microglia.

$CD8^+$ cell density in the BLA also differed significantly among groups (one-way ANOVA, $F(2,6) = 56.9$, $P = 0.0001$; Fig. 7d,f). R94W+Veh mice exhibited a marked increase in $CD8^+$ cells compared with Ctrl+Veh mice ($P < 0.001$), whereas Gi-DREADD activation reduced $CD8^+$ cell accumulation in the R94W BLA ($P < 0.01$). The parallel changes in microglial CXCL10 signal and $CD8^+$ cell density, together with transcriptomic

enrichment of chemokine- and T-cell-related programs, support an association between the R94W microglial state and adaptive immune-cell accumulation.

The parallel transcriptomic and imaging changes identify a CXCL10-associated microglia–$CD8^+$ cell response in the R94W BLA that is sensitive to Gi-DREADD activation. These data establish an association, however, and do not by themselves demonstrate direct CXCL10-dependent recruitment of $CD8^+$ cells.

R94W mice exhibit enhanced TLR4–MYD88–NF-κB-associated inflammatory signaling that is attenuated by Gi-DREADD activation

KEGG enrichment analysis showed that genes upregulated in the R94W BLA were enriched in cytokine–cytokine receptor interactions, chemokine, TNF, JAK–STAT, Toll-like receptor, NOD-like receptor, NF-κB, IL-17, and phagosome pathways (adjusted $P < 0.05$; Fig. 8a). Many of these pathways were enriched among genes downregulated following Gi-DREADD activation, indicating broad attenuation of the R94W-associated inflammatory transcriptional state (Fig. 8b). Consistent with these pathway-level changes, a heatmap based on group-averaged expression showed coordinated alterations in immune-, inflammatory-, and serotonergic-pathway-related DEGs in R94W mice, many of which shifted toward control levels following Gi-DREADD activation (Fig. 8c). The expression patterns across individual RNA-sequencing samples are shown in Supplementary Fig. 6a, and RT–qPCR further validated selected pathway-related transcripts (Supplementary Fig. 6b).

We next examined TLR4–MYD88–NF-κB-associated signaling at the cellular and protein levels. MYD88 immunoreactivity within mCherry-positive microglia differed significantly among groups (one-way ANOVA, $F(2,6) = 40.16$, $P = 0.0003$; Fig. 8d,f). Microglial MYD88 intensity was increased in R94W+Veh mice compared with Ctrl+Veh mice ($P < 0.001$) and was reduced following Gi-DREADD activation ($P < 0.01$). Consistently, total BLA MYD88 abundance differed among groups ($F(2,6) = 24.82$, $P = 0.0013$; Fig. 8g), increasing in R94W+Veh mice relative to controls ($P < 0.01$) and decreasing after Gi-DREADD activation ($P < 0.01$). Western blotting further showed that TLR4 protein abundance was increased in R94W+Veh mice relative to Ctrl+Veh mice ($P < 0.01$) and was reduced following Gi-DREADD activation ($P < 0.05$; Fig. 8g).

NF-κB p65 immunoreactivity within mCherry-positive microglia also differed significantly among the groups (one-way ANOVA, $F(2,6) = 296.0$, $P < 0.0001$; Fig. 8e,h). R94W+Veh mice showed markedly increased microglial NF-κB p65 intensity compared with Ctrl+Veh mice ($P < 0.001$), whereas Gi-DREADD activation significantly reduced this signal ($P < 0.001$). Three-dimensional imaging of MYD88 and NF-κB p65, together with complementary NLRP3 immunofluorescence, provided additional spatial support for the Gi-sensitive inflammatory microglial phenotype (Supplementary Fig. 6d–e).

These results link the R94W phenotype to coordinated inflammatory pathway enrichment, increased BLA TLR4 and MYD88 abundance, and enhanced NF-κB p65 signaling in microglia. Each of these changes was attenuated by Gi-DREADD activation.

AMG487 treatment ameliorates anxiety-related behavioral and CXCL10-associated neuroimmune abnormalities in R94W mice

To pharmacologically investigate the potential contribution of CXCL10-associated signaling, we treated R94W mice with AMG487, a CXCR3 antagonist, and assessed behavioral and neuroimmune outcomes. Open-arm duration differed significantly among groups (one-way ANOVA, $F(2,29) = 3.884$, $P = 0.0320$; Fig. 9a). R94W mice spent less time in the open arms than WT mice ($P < 0.05$), whereas AMG487 shifted open-arm duration toward the WT level without producing a significant difference relative to untreated R94W mice. Closed-arm duration did not differ significantly among groups ($F(2,29) = 3.204$, $P = 0.0553$). The open-arm-to-total-arm duration ratio was also reduced in R94W mice compared with WT controls ($F(2,29) = 3.749$, $P =$

0.0356; $P < 0.05$), whereas AMG487 produced a nonsignificant shift toward the control value. Thus, the effect of AMG487 on elevated-plus-maze performance was partial.

In contrast, marble-burying behavior differed significantly among the groups (one-way ANOVA, $F(2,29) = 8.496$, $P = 0.0012$; Fig. 9b). R94W mice buried significantly more marbles than WT controls ($P < 0.01$), and AMG487 treatment significantly reduced marble burying relative to untreated R94W mice ($P < 0.01$).

$CD8^+$ cell density in the BLA also showed a significant overall group difference (one-way ANOVA, $F(2,6) = 38.74$, $P = 0.0004$; Fig. 9c,e). R94W mice exhibited markedly increased $CD8^+$ cell accumulation compared with WT mice ($P < 0.001$), which was significantly reduced following AMG487 treatment ($P < 0.01$). Similarly, CXCL10 intensity within Iba1-positive microglial regions differed significantly among the groups (one-way ANOVA, $F(2,6) = 28.47$, $P = 0.0009$; Fig. 9d,f). Microglial CXCL10 signal was increased in R94W mice relative to WT controls ($P < 0.001$) and was significantly reduced by AMG487 treatment ($P < 0.01$).

Representative images showed reduced spatial overlap of Iba1-positive microglia with SYP- and PSD95-positive synaptic material after AMG487 treatment, providing qualitative support for attenuation of microglia-associated synaptic cargo (Supplementary Fig. 7). Because these observations were not quantified, they were not used to establish a treatment effect on synaptic engulfment.

AMG487 reduced marble burying and partially improved elevated-plus-maze performance. The accompanying decreases in BLA $CD8^+$ T-cell accumulation and microglial CXCL10 signal provide pharmacological support for the involvement of **CXCL10-associated signaling** in the neuroimmune phenotype of R94W mice.

Exploratory TRP-channel and human CMT2A analyses support broader MFN2-associated remodeling

Exploratory screening of all TRP-channel genes in the BLA RNA-sequencing dataset identified statistically significant changes only in *Trpv4*, *Trpv6*, and *Trpm3*, with *Trpv4* showing the strongest statistical difference. Given the established mechanosensitive properties of TRPV4, we further examined selected mechanosensing- or mechanotransduction-related channels, including *Piezo1*, *Trpm2*, and *Trpm7*; none showed significant expression changes (Supplementary Fig. 8b). In BV2 cells, LPS stimulation increased TRPV4 protein abundance (*t*-test, $t = 7.514$, $P = 0.0017$), supporting inflammation-sensitive regulation of TRPV4 expression (Supplementary Fig. 8c–e). BLA TRPV4 immunoreactivity was reduced in R94W mice and increased following Gi-DREADD activation ($F(2,6) = 384.1$, $P < 0.0001$); however, TRPV4 showed limited spatial overlap with mCherry-positive microglia (Supplementary Fig. 8f,g). Accordingly, these findings were considered exploratory and TRPV4 was not incorporated into the core microglial mechanism.

To examine whether inflammatory and metabolic pathway changes were also detectable in human CMT2A-derived cells, we analyzed a public transcriptomic dataset of CMT2A patient fibroblasts. Gene-set enrichment analysis showed positive enrichment of interferon-γ response, TNF–NF-κB signaling, inflammatory response, antigen processing and presentation, Toll-like receptor signaling, phagosome, and complement pathways, together with negative enrichment of oxidative phosphorylation (Supplementary Fig. 9). Although fibroblasts and BLA microglia are biologically distinct, these findings provide supportive, cross-context evidence for an association between MFN2 dysfunction, inflammatory transcriptional remodeling, and altered oxidative phosphorylation.

Discussion

Our data identify BLA microglial dysregulation as a potential contributor to behavioral abnormalities associated with MFN2 R94W. Mfn2 R94W mutant mice displayed anxiety-related, depression-related, and marble-burying/grooming phenotypes, suggesting that the consequences of MFN2 dysfunction may extend

beyond peripheral axons. Gi-DREADD activation in BLA CX3CR1-targeted cells improved open-field and elevated-plus-maze measures, while also reducing marble burying, across two targeting strategies. In contrast, Gq-DREADD activation showed no consistent benefit. These findings are consistent with our earlier observation that regional chemogenetic inhibition of BLA microglia improved socio-emotional behavior after sleep deprivation, whereas global microglial depletion did not provide a comparable rescue [14]. Our findings are also consistent with studies showing that amygdalar microglia regulate anxiety-related behavior through synaptic engulfment, although their effects may vary across stress conditions and amygdala subregions [16, 17]. Together, these observations suggest that region-specific microglial states may influence amygdala-dependent behavior.

The findings may also be relevant to the psychological burden of CMT. An Italian national-registry study reported increased depression and psychological distress, with greater disease severity and sensory symptoms associated with poorer outcomes [5]. Neurological disability also affects quality of life[18]. Although these manifestations are commonly attributed to disability, pain, and chronic disease, our findings raise the possibility that central neuroimmune alterations may also contribute.

Immunofluorescence and Western blotting showed increased Iba1 signal and protein abundance in the BLA of R94W mice. Three-dimensional morphometry further revealed increased microglial volume and surface area, whereas the surface-area-to-volume ratio remained unchanged. These structural changes should be interpreted alongside the functional and transcriptional data, given the diversity of microglial states [19].

Gi-DREADD-mediated inhibition of BLA microglia improved behavioral abnormalities, supporting a contribution of altered microglial states. GSEA and KEGG analyses identified enhanced phagocytosis-related programs in R94W mice that were attenuated following Gi-DREADD activation. Consistent with these transcriptional changes, SYP- and PSD95-positive material was increased within microglial regions. Three-dimensional images and rotational videos further supported the intracellular localization of PSD95. Together, these findings suggest enhanced microglial synaptic engulfment, in line with reports of pathological microglia-mediated synapse removal in other disease models [20]. However, transcriptomic and Western blot analyses did not provide evidence for widespread synaptic loss in the BLA, suggesting that the observed changes may reflect more localized synaptic remodeling.

The mitochondrial findings further suggest accompanying metabolic remodeling. Transcriptomic changes in mitochondria-related pathways occurred without detectable changes in bulk BLA respiratory-chain complexes I, II, III, or V. In contrast, COX IV immunoreactivity increased within mCherry-positive microglia and was reduced after Gi-DREADD activation, suggesting a microglia-associated response rather than a uniform mitochondrial increase across the BLA. Microglial metabolism is closely linked to phagocytosis [21, 22], and mitochondrial complex I activity can support inflammatory microglial states[10]. Thus, the metabolic and redox-related transcriptional changes observed in the R94W BLA may accompany the altered phagocytic and inflammatory state. The differing COX IV patterns in bulk tissue and microglia further support cell-type-associated mitochondrial adaptation.

Together with the pathway-enrichment results, the TLR4–MYD88–NF-κB-associated findings support the involvement of altered innate immune signaling in the R94W BLA. MYD88 transduces signals from most Toll-like receptor signaling and can activate NF-κB-dependent transcription [11, 23, 24]. R94W mice showed increased BLA TLR4 protein abundance together with increased MYD88 and NF-κB p65 signals within mCherry-positive microglia, and Gi-DREADD activation attenuated these changes, paralleling enrichment of Toll-like receptor, NOD-like receptor, and cytokine-response programs.

This study combined the use of complementary disease models and microglial targeting strategies. Related behavioral abnormalities were observed in two disease-associated *Mfn2* mutant models, T105M and R94W,

indicating that the central behavioral phenotype was not restricted to a single *Mfn2* variant. The more robust phenotype of R94W mice provided the basis for subsequent mechanistic studies. Importantly, the beneficial effects of microglial Gi-DREADD activation were validated using two complementary approaches: CX3CR1 promoter-based viral targeting in R94W mice and Cre-dependent viral targeting in Cx3cr1-*Cre* × R94W mice. The agreement between the viral and genetic approaches supports the conclusion that BLA CX3CR1-expressing microglia contribute to the behavioral phenotype. Future cell-type-specific genetic studies will further define the causal contribution of the identified microglial mechanisms. Reanalysis of GSE158650 provided additional pathway-level support by showing inflammatory enrichment in CMT2A fibroblasts [25].

MFN2 R94W was associated with a distinct BLA microglial state that included altered COX IV immunoreactivity, increased synaptic cargo, TLR4–MYD88–NF-κB-associated inflammation, CXCL10 induction, and $CD8^+$ T-cell accumulation. Microglial Gi-DREADD activation attenuated these features and improved behavioral outcomes, whereas CXCR3 antagonism produced a partial behavioral and neuroimmune rescue. The findings broaden the pathophysiological framework of CMT2A beyond peripheral axons and identify regional microglial and chemokine states as candidate contributors to central behavioral manifestations. Cell-specific experiments and clinical validation will be required to establish their causal and translational relevance.

Materials and Methods

Animals and genotyping

Mfn2$^{R94W/+}$ knock-in mice and *Mfn2*$^{T105M/+}$ mice bred and maintained by our research team. *Cx3cr1*-Cre mice were kindly provided by Jiawei Zhou (University of Chinese Academy of Sciences, China). and corresponding littermate controls were maintained under specific-pathogen-free conditions with controlled temperature and humidity on a 12-h light/dark cycle. Food and water were available *ad libitum*. Mice were randomly assigned to experimental groups. All procedures were approved by the Nankai University Animal Research Ethics Committee (approval no. 2022-SYDWLL-000019).

Stereotaxic viral injection

Mice were anesthetized and placed in a stereotaxic frame. Viruses were delivered bilaterally into the BLA. AAV2/9-*Cx3cr1*-Cre-3×FLAG and Cre-dependent adeno-associated virus (AAV) vectors (serotype 2/9) were obtained from Hanbio Biotechnology Co., Ltd. (Shanghai, China).

In the initial chemogenetic experiment, AAV2/9-*Cx3cr1*-Cre-3×FLAG was co-injected with AAV2/9-CAG-DIO-hM3D(Gq)-mCherry or AAV2/9-CAG-DIO-hM4D(Gi)-mCherry. In the genetic-cross experiment, AAV2/9-CAG-DIO-hM4D(Gi)-mCherry was injected into *Cx3cr1*-Cre-positive control and *Mfn2* R94W mice. Behavioral testing began three weeks after viral injection.

Viral vectors were supplied in sterile phosphate-buffered saline at titers of $\geq 1.0 \times 10^{12}$ vector genomes (vg)/mL, as determined by quantitative PCR, and were certified as endotoxin-free and replication-deficient. Mice were anesthetized with tribromoethanol and positioned in a stereotaxic apparatus (RWD Life Science Co., Ltd., China). Using a 2-μL microsyringe, 0.5 μL of viral suspension per hemisphere was injected bilaterally into the BLA at the following coordinates relative to bregma: anteroposterior, −1.82 mm; mediolateral, ±2.70 mm; and dorsoventral, −4.60 mm. After each injection, the needle was left in place for 5 min to minimize reflux before being slowly withdrawn. Mice were individually housed for one week after surgery to facilitate postoperative recovery.

Chemogenetic activation

Clozapine N-oxide (CNO; MCE, HY-17366) was administered (*i.p.*, 1 mg/kg) 30 min before behavioral testing to activate hM4D(Gi) or hM3D(Gq). Vehicle-treated animals underwent identical handling and received matched intraperitoneal injections.

AMG487 administration

AMG487, a CXCR3 antagonist, was purchased from Aladdin Biochemical Technology Co., Ltd. (China). R94W mice received AMG487 (*i.p.*, 5 mg/kg) once daily for 14 consecutive days. WT control mice and vehicle-treated R94W mice received an equivalent volume of vehicle (5% DMSO in 0.9% normal saline) according to the same schedule. Behavioral testing began 1 h after the final injection, and tissue samples were collected after completion of the behavioral experiments.

Behavioral testing

Behavioral tests were conducted in a dedicated testing room under controlled environmental conditions. Mice were acclimated to the testing room before each test. Behavior was recorded using a video-tracking system and analyzed by an investigator blinded to group allocation. All apparatuses were cleaned with 70% ethanol between animals to minimize residual olfactory cues.

Open-field test

The open-field apparatus consisted of a square arena (60 × 60 cm) with 40-cm-high walls and was divided into 16 equal squares. The four central squares constituted a 30 × 30-cm center zone, and the remaining area was defined as the peripheral zone. After 1–2 min of habituation period, each mouse was placed in the center and allowed to explore freely for 5 min. Activity time, center-zone duration, center entries, total distance travelled, and distance travelled within the center zone were quantified.

Elevated-plus-maze test

The elevated plus maze consisted of two open arms and two closed arms with 20-cm-high walls, arranged orthogonally and elevated 40 cm above the floor. Each mouse was placed in the central platform facing an open arm and allowed to explore for 5 min. The time spent in and number of entries into the open and closed arms were recorded. Open-to-closed-arm ratios for duration and entries were subsequently calculated.

Marble-burying test

Each mouse was individually placed in a cage containing 5 cm of fresh bedding with 21 glass marbles evenly arranged on the surface. Mice were allowed to explore for 30 min without prior habituation. A marble was considered buried when at least two-thirds of its surface was covered by bedding. The number of buried marbles was scored by an investigator blinded to group allocation.

Spontaneous grooming test

Mice were individually placed in a transparent observation chamber and allowed to habituate for 5 min. Grooming behavior was then recorded for 30 min. A grooming bout was defined as a continuous sequence of face washing, body grooming, limb licking, or tail/genital grooming; interruptions lasting longer than 2 s were considered the start of a new bout. The number of grooming bouts was quantified by an investigator blinded to group allocation.

Tail-suspension test

Mice were suspended by the tail using adhesive tape attached approximately 1 cm from the tail tip, at a height of 30 cm above the floor. Behavior was recorded for 6 min, and immobility during the final 5 min was

quantified. Immobility was defined as the absence of active escape-directed movements, excluding movements caused by respiration.

Forced-swim test

Mice were individually placed in a transparent cylindrical container (20 cm in diameter and 40 cm in height) filled with water to a depth of 20 cm at 25 ℃. Each test lasted 6 min, and immobility during the final 5 min was quantified. Immobility was defined as the absence of active escape-directed movements, with only minimal movements required to keep the head above water. After testing, mice were dried and returned to a warmed recovery cage before being returned to their home cages.

Tissue processing and immunofluorescence

Mice were deeply anesthetized with tribromoethanol (250 mg/kg, *i.p*). After complete loss of the pedal withdrawal reflex, mice were transcardially perfused with ice-cold 0.9% saline, followed by 4% paraformaldehyde (PFA) in 0.1 M phosphate buffer (PB; pH 7.4). Brains were removed, post-fixed in 4% PFA at 4 ℃ for 24 h, and subsequently immersed in 30% sucrose in 0.1 M PB at 4 ℃ until they sank. Coronal brain sections (20 μm) were prepared using a vibratome and collected in phosphate-buffered saline for free-floating immunofluorescence staining.

For immunofluorescence staining, brain sections were permeabilized with 0.3% Triton X-100 in PBS for 3 min and blocked with 10% normal goat serum for 1 h at room temperature. Sections were incubated with the indicated primary antibodies overnight at 4 ℃ in a humidified chamber, followed by the appropriate fluorophore-conjugated secondary antibodies for 1 h at room temperature. Primary antibody information, including suppliers, catalog numbers, and working dilutions, is provided in Table 1.

Images were acquired using an Olympus BX53 fluorescence microscope (Olympus, Japan) or a Leica TCS SP5 laser-scanning confocal microscope (Leica Microsystems, Germany). Within each experiment, acquisition parameters were kept constant across groups. 3-5 non-overlapping fields were sampled from predefined brain regions of each mouse using a systematic sampling procedure. Field-level measurements were averaged to obtain a single biological replicate per mouse.

Image quantification and three-dimensional analysis

Image analysis was performed using ImageJ/Fiji by an investigator blinded to group allocation. Background-subtraction and thresholding parameters were determined using representative images and then kept constant across all images within the same experiment. Confocal Z-stacks of mCherry-positive microglia were acquired at 1-μm intervals and reconstructed using identical settings. Three-dimensional microglial morphology was quantified as cell surface area (μm^2), cell volume (μm^3), and surface-area-to-volume ratio (μm^{-1}). For three-dimensional morphological analysis, 10–49 microglial cells per mouse were analyzed.

SYP- and PSD95-positive puncta were quantified in two-dimensional images using consistent size and intensity criteria. Puncta located within the boundaries of mCherry-positive microglial profiles were quantified as the number of microglia-associated puncta per cell and the percentage of the mCherry-positive area occupied by puncta. Three-dimensional rotational renderings of PSD95-positive puncta within mCherry-positive microglial volumes were used only for qualitative visualization and were not included in the statistical analysis. COX IV, CXCL10, MYD88, and NF-κB p65 fluorescence intensities were measured within mCherry-positive regions, whereas CXCL10 intensity in the AMG487 experiment was measured within Iba1-positive regions. Iba1-positive area and CD8-positive cell number were also quantified. For analyses other than three-dimensional morphology, 3–5 non-overlapping fields were evaluated per mouse. Three mice were analyzed

per group. Cell- or field-level measurements were averaged to obtain one biological value per mouse, and the mouse was treated as the statistical unit.

BLA-enriched amygdala tissue collection

Mice were deeply anesthetized and euthanized, after which the brains were rapidly removed and placed on an ice-cold surface. Coronal brain slices (1 mm thick) were prepared using a mouse brain matrix. Slices containing the amygdala, spanning approximately −0.94 to −2.54 mm relative to bregma, were identified according to a mouse brain atlas. Amygdala tissue was microdissected under a stereomicroscope (Olympus SZX16, Japan) on an ice-cold metal plate and immediately collected for subsequent molecular analyses.

Western blotting

Amygdala tissues were homogenized in ice-cold RIPA lysis buffer supplemented with protease inhibitors. BV2 cells were washed with ice-cold PBS and lysed using the same buffer. Lysates were centrifuged at 4 ℃, and supernatants were collected for protein quantification using a BCA assay. Equal amounts of protein (10 μg per lane) were separated by 10% SDS–PAGE according to target size and transferred to polyvinylidene difluoride membranes. Membranes were incubated with primary antibodies overnight at 4 ℃ and with the appropriate secondary antibodies for 1 h at room temperature. Bands were visualized by enhanced chemiluminescence, quantified using ImageJ, and normalized to β-actin or GAPDH as indicated. Antibody information is provided in Table 1.

BV2 cell culture and LPS stimulation

BV2 microglial cells were kindly provided by Leiting Pan (Nankai University, Tianjin, China). Cells were maintained in DMEM/F12 supplemented with 10% fetal bovine serum (FBS), 100 U/mL penicillin, and 100 μg/mL streptomycin at 37°C in a humidified atmosphere containing 5% CO_2. For dose-ranging experiments, cells were treated with LPS (Aladdin Biochemical Technology Co., Ltd., China) at 100 ng/mL, 500 ng/mL, or 1 μg/mL for 24 h. Independent cultures were treated with 1 μg/mL LPS for 24 h to validate the selected condition. Cells were then harvested, and TRPV4 protein abundance was assessed by Western blotting.

Bulk RNA sequencing and bioinformatic analysis

BLA tissue was collected from Ctrl+Veh, R94W+Veh, and R94W+Gi mice for bulk RNA sequencing. Differential-expression analyses compared R94W+Veh with Ctrl+Veh and R94W+Gi with R94W+Veh. Unless otherwise indicated, differentially expressed genes were defined by |log (fold change)| > 1 and adjusted $P < 0.05$. GO and KEGG over-representation analyses were performed on the indicated differentially expressed gene sets, and GO-based GSEA was performed using ranked gene lists. Heatmaps display row-scaled normalized expression.

Total RNA was extracted from BLA tissue using TransZol Up reagent. RNA integrity was assessed by 1.5% agarose-gel electrophoresis or fragment analysis, and RNA purity was evaluated using a NanoDrop spectrophotometer. Polyadenylated RNA was enriched using oligo(dT) magnetic beads, and sequencing libraries were prepared using the VAHTS Universal V8 RNA-seq Library Prep Kit for Illumina. Libraries were quantified using a Qubit 4.0 fluorometer and sequenced on an Illumina NovaSeq 6000 platform. The nine samples generated 72.88 Gb of clean data in total, corresponding to an average of approximately 8.10 Gb per sample; Q30 values ranged from 97.77% to 98.43%.

Raw reads were processed using fastp v0.23.2 to remove adapter sequences, low-quality bases, short reads, and reads containing ambiguous nucleotides. Clean reads were aligned to the mouse reference genome GRCm39 (Ensembl release 106) using STAR v2.7.7a. Transcript abundance was quantified using StringTie

v2.0.0, and gene-level expression was summarized as raw counts and TPM values. Differential expression analysis was performed using edgeR, with sequencing-depth normalization applied to the raw count data. Genes with an absolute $\log_2$ fold change >1 and a Benjamini–Hochberg-adjusted *P* value <0.05 were considered differentially expressed.

GO-based GSEA was performed using clusterProfiler v4.0.2 on approximately 16,600 quantified genes ranked according to the differential-expression results. Benjamini–Hochberg-adjusted *P* values < 0.05 were considered statistically significant.

Cell-type expression profiles and UMAP feature plots of *Mfn2* and *Aif1* were generated using the built-in online analysis tools of the Allen Brain Cell Atlas [26](accessed March 2026).

Reanalysis of public human CMT2A fibroblast transcriptomic data

Publicly available human fibroblast RNA-sequencing data were obtained from the Gene Expression Omnibus (GEO; accession GSE158650). The reanalyzed dataset included three healthy-control fibroblast lines and two CMT2A fibroblast lines carrying the *Mfn2* R274W or H361Y variant. After gene-identifier harmonization, GSEA was performed using GSEA v4.3.2, with genes ranked according to signal-to-noise metric. Enrichment was assessed against the MSigDB Hallmark gene sets (v7.5.1). Positive NESs indicate enrichment toward genes more highly expressed in CMT2A fibroblasts, whereas negative NESs indicate enrichment toward genes more highly expressed in control fibroblasts. Statistical significance was evaluated using nominal *P* values and FDR *q* values.

Statistical analysis

Data are presented as mean ± SEM. Each dot represents one mouse unless otherwise stated; imaging values were averaged within each mouse before group-level analysis. Comparisons between two independent groups were performed using an unpaired two-tailed Student's *t*-test. Multi-group analyses were performed using one-way or two-way ANOVA followed by Tukey's or Šídák's multiple-comparisons test specified in the corresponding figure legend. Statistical significance was defined as $P < 0.05$.

Data availability

The publicly available human fibroblast RNA-seq dataset re-analyzed in this study was downloaded from the Gene Expression Omnibus (GEO) under accession number GSE158650. The raw and processed bulk BLA RNA-seq data generated in the present study have been deposited in GEO under accession number GSE345566. Uncropped Western blot images are provided in Supplementary Data 1. All numerical raw data are available from the corresponding author upon reasonable request.

Acknowledgements

We thank Dr. Leiting Pan for providing the BV2 cells and Dr. Jiawei Zhou for providing the *Cx3cr1*-Cre mice.

Author contributions

S.Z. and Y.T.L. performed the majority of the experiments, analyzed the data, and organized the experimental results. R.S., T.X., D.K., and B.H. performed experiments. Y.C. provided methodological guidance for the immunofluorescence experiments. Y.L. supervised the experimental work. G.C. contributed to project coordination and supervision. Z.W.L. conceived and designed the study, organized and interpreted the data, and wrote the manuscript. All authors reviewed and approved the final manuscript.

Competing interests

The authors declare no competing interests.

Declaration of generative AI use

The authors used ChatGPT (OpenAI) for language editing and improving manuscript clarity. All output was critically reviewed and revised by the authors, who take full responsibility for the final manuscript.

References

1. Zuchner, S., et al., *Mutations in the mitochondrial GTPase mitofusin 2 cause Charcot-Marie-Tooth neuropathy type 2A.* Nat Genet, 2004. **36**(5): p. 449-51.
2. Xie, Y., et al., *MFN2-related genetic and clinical features in a cohort of Chinese CMT2 patients.* J Peripher Nerv Syst, 2016. **21**(1): p. 38-44.
3. Ando, M., et al., *Nationwide Characterization of MFN2-Related CMT in 176 Japanese Patients: Clinical and Genetic Insights.* Ann Clin Transl Neurol, 2026. **13**(1): p. 170-179.
4. Weigele, J., A. Franco, and G.W. Dorn, 2nd, *Neuromuscular Dysfunction and Charcot-Marie-Tooth Disease Reversal in Mfn2 T105M Knock-In Rats.* Int J Mol Sci, 2026. **27**(16).
5. Bellofatto, M., et al., *Anxiety and depression in Charcot-Marie-Tooth disease: data from the Italian CMT national registry.* J Neurol, 2023. **270**(1): p. 394-401.
6. Gebara, E., et al., *Mitofusin-2 in the Nucleus Accumbens Regulates Anxiety and Depression-like Behaviors Through Mitochondrial and Neuronal Actions.* Biol Psychiatry, 2021. **89**(11): p. 1033-1044.
7. Ghosal, S., et al., *Mitofusin-2 in nucleus accumbens D2-MSNs regulates social dominance and neuronal function.* Cell Rep, 2023. **42**(7): p. 112776.
8. Paolicelli, R.C., et al., *Synaptic pruning by microglia is necessary for normal brain development.* Science, 2011. **333**(6048): p. 1456-8.
9. Schafer, D.P., et al., *Microglia sculpt postnatal neural circuits in an activity and complement-dependent manner.* Neuron, 2012. **74**(4): p. 691-705.
10. Peruzzotti-Jametti, L., et al., *Mitochondrial complex I activity in microglia sustains neuroinflammation.* Nature, 2024. **628**(8006): p. 195-203.
11. Deguine, J. and G.M. Barton, *MyD88: a central player in innate immune signaling.* F1000Prime Rep, 2014. **6**: p. 97.
12. Chen, X., et al., *Microglia-mediated T cell infiltration drives neurodegeneration in tauopathy.* Nature, 2023. **615**(7953): p. 668-677.
13. Groh, J., et al., *Microglia activation orchestrates CXCL10-mediated CD8(+) T cell recruitment to promote aging-related white matter degeneration.* Nat Neurosci, 2025. **28**(6): p. 1160-1173.
14. Xin, T., et al., *Microglial inhibition in the basolateral amygdala is associated with improved socio-emotional behaviors following sleep deprivation in mice.* Brain Res, 2026. **1885**: p. 150332.

15. Verhoeven, K., et al., *MFN2 mutation distribution and genotype/phenotype correlation in Charcot-Marie-Tooth type 2.* Brain, 2006. **129**(Pt 8): p. 2093-102.
16. Peng, X., et al., *Microglial activation in the lateral amygdala promotes anxiety-like behaviors in mice with chronic moderate noise exposure.* CNS Neurosci Ther, 2024. **30**(3): p. e14674.
17. Chen, D., et al., *Microglia govern the extinction of acute stress-induced anxiety-like behaviors in male mice.* Nat Commun, 2024. **15**(1): p. 449.
18. Padua, L., et al., *Variables influencing quality of life and disability in Charcot Marie Tooth (CMT) patients: Italian multicentre study.* Neurol Sci, 2006. **27**(6): p. 417-23.
19. Hammond, T.R., et al., *Single-Cell RNA Sequencing of Microglia throughout the Mouse Lifespan and in the Injured Brain Reveals Complex Cell-State Changes.* Immunity, 2019. **50**(1): p. 253-271 e6.
20. Hong, S., et al., *Complement and microglia mediate early synapse loss in Alzheimer mouse models.* Science, 2016. **352**(6286): p. 712-716.
21. Ulland, T.K., et al., *TREM2 Maintains Microglial Metabolic Fitness in Alzheimer's Disease.* Cell, 2017. **170**(4): p. 649-663 e13.
22. Baik, S.H., et al., *A Breakdown in Metabolic Reprogramming Causes Microglia Dysfunction in Alzheimer's Disease.* Cell Metab, 2019. **30**(3): p. 493-507 e6.
23. Kawai, T. and S. Akira, *The role of pattern-recognition receptors in innate immunity: update on Toll-like receptors.* Nat Immunol, 2010. **11**(5): p. 373-84.
24. O'Neill, L.A., D. Golenbock, and A.G. Bowie, *The history of Toll-like receptors - redefining innate immunity.* Nat Rev Immunol, 2013. **13**(6): p. 453-60.
25. Dang, X., et al., *Mitochondrial Phenotypes in Genetically Diverse Neurodegenerative Diseases and Their Response to Mitofusin Activation.* Cells, 2022. **11**(6).
26. Yao, Z., et al., *A high-resolution transcriptomic and spatial atlas of cell types in the whole mouse brain.* Nature, 2023. **624**(7991): p. 317-332.

Figure legends

Figure 1. Behavioral phenotypes of *Mfn2* mutant mice. (a) Schematic of heterozygous *Mfn2* T105M/+ and *Mfn2* $^{R94W/+}$ mice. (b) Number of marbles buried in the marble-burying test. (c) Number of grooming bouts. (d) Immobility time in the tail-suspension test. (e) Representative elevated-plus-maze (EPM) trajectories; OA, open arms; CA, closed arms. (f) Quantification of open- and closed-arm duration and entries and the corresponding open-arm/closed-arm ratios. Data are mean ± SEM; each dot represents one mouse. One-way ANOVA followed by Tukey's multiple-comparisons test. *$P < 0.05$, **$P < 0.01$, and ***$P < 0.001$.

Figure 2. Effects of chemogenetic modulation of BLA CX3CR1-targeted cells on behavior in *Mfn2* $^{R94W/+}$ mice. (a) Bilateral viral injection into the BLA and representative expression. (b) Representative images evaluating overlap of mCherry with NeuN or GFAP; nuclei were counterstained with DAPI. (c) Percentages of mCherry-positive cells colabeled with NeuN or GFAP. (d) Experimental timeline. (e) Representative open-field trajectories. (f) Quantification of activity time, center duration, total distance, and center distance. (g) EPM measurements. (h) Representative EPM trajectories. Data are mean ± SEM; each dot represents one mouse. Data were analyzed using two-way ANOVA followed by Šídák's multiple-comparisons test. *$P <$ 0.05 and **$P < 0.01$; exact P values are shown.

Figure 3. Microglial Gi-DREADD activation attenuates altered COX IV immunoreactivity and synaptic cargo in *Mfn2* $^{R94W/+}$ mice. (a) Representative Western blots of mitochondrial respiratory-chain complexes I, II, III, and V. (b) Densitometric quantification normalized to GAPDH. (c) SYP Western blots and quantification. (d) Mean COX IV fluorescence intensity within mCherry-positive microglia. (e) Internalized SYP-positive area as a percentage of mCherry-positive microglial area. (f) Proposed relationship among the microglial mitochondrial state, synaptic engulfment, and neuronal dysfunction. (g,h) Representative COX IV and SYP images. Data are mean ± SEM; imaging values are per-mouse means calculated from three fields. **$P < 0.01$ and ***$P < 0.001$.

Figure 4. Microglial Gi-DREADD activation attenuates anxiety-related behavioral abnormalities in *Mfn2* $^{R94W/+}$ mice. (a) Experimental timeline. (b) Bilateral BLA injection of AAV2/9-CAG-DIO-hM4D(Gi)-mCherry and representative expression. (c) Representative EPM trajectories and quantification of open- and closed-arm measures. (d) Marble-burying test. (e) GO enrichment analysis of genes upregulated in R94W+Gi mice relative to R94W+Veh mice (adjusted $P < 0.05$). Behavioral data are mean ± SEM; each dot represents one mouse. One-way ANOVA followed by Tukey's multiple-comparisons test. *$P < 0.05$, **$P < 0.01$, and ***$P < 0.001$.

Figure 5. BLA transcriptomics reveals immune and inflammatory alterations in *Mfn2* $^{R94W/+}$ mice and their modulation by microglial Gi-DREADD activation. (a) Bulk RNA-sequencing workflow. (b) Venn diagram showing shared and unique differentially expressed genes among the indicated comparisons. (c) Volcano plot and heatmap for R94W+Veh versus Ctrl+Veh. (d) Heatmap and volcano plot for R94W+Gi versus R94W+Veh. Red and green indicate upregulated and downregulated genes, respectively; gray indicates nonsignificant genes. Heatmap colors show row-scaled normalized expression. Differentially expressed genes were defined by $|\log_2(\text{fold change})| > 1$ and adjusted $P < 0.05$. (e,f) GO enrichment analyses for the indicated upregulated or downregulated gene sets. (g,h) KEGG enrichment analyses; bubble size indicates gene number, color indicates *P* value, and the x axis shows enrichment score.

Figure 6. Microglial Gi-DREADD activation attenuates microglial morphological alterations and synaptic engulfment in *Mfn2*$^{R94W/+}$ mice.
(a) Representative confocal images of mCherry-labeled BLA microglia from the Ctrl+Veh, R94W+Veh, and R94W+CNO groups. Scale bar, 10 μm. (b) Three-dimensional quantification of microglial soma volume, soma surface area, and surface area-to-volume ratio. (c) Gene set enrichment analysis (GSEA) of leukocyte-mediated immunity and phagocytic-vesicle-related gene sets. These gene sets were positively enriched in R94W+Veh mice compared with Ctrl+Veh mice and negatively enriched in R94W+CNO mice compared with R94W+Veh mice. Normalized enrichment scores (NES) and adjusted *P* values are shown. (d) Representative confocal images showing SYP-positive or PSD95-positive puncta (green) within mCherry-positive microglia (red) in the indicated groups. Nuclei were counterstained with DAPI (blue). Scale bar, 10 μm. (e) Quantification of the numbers of internalized SYP-positive and PSD95-positive puncta per microglial cell. (f) Representative higher-magnification images showing PSD95-positive puncta within mCherry-positive microglia from R94W+Veh and R94W+CNO mice. Nuclei were counterstained with DAPI. Scale bar, 10 μm. Data are presented as mean ± SEM. For immunofluorescence analyses, each dot represents the mean value from one mouse, calculated from three fields of view. Statistical significance was assessed using one-way ANOVA followed by Tukey's multiple-comparisons test. *$P < 0.05$, **$P < 0.01$, and ***$P < 0.001$.

Figure 7. Microglial Gi-DREADD activation reduces CXCL10 expression and $CD8^+$ T-cell accumulation in the BLA of *Mfn2* $^{R94W/+}$ mice. (a) Proposed chemokine-associated model. (b) Heatmaps of antigen-presentation-, chemokine-, and $CD8^+$ T-cell-activation-related differentially expressed genes. (c) Mean CXCL10 intensity in mCherry-positive microglia. (d) $CD8^+$ cells per square millimeter in the BLA. (e) Representative CXCL10 images. (f) Representative distribution of $CD8^+$ cells relative to mCherry-positive microglia. Data are mean ± SEM; each dot represents a per-mouse mean. One-way ANOVA followed by Tukey's test. **$P < 0.01$ and ***$P < 0.001$.

Figure 8. Microglial Gi-DREADD activation suppresses TLR4/MYD88/NF-κB-associated inflammatory signaling in the BLA of Mfn2 R94W/+ mice. (a,b) Representative KEGG pathways enriched among genes upregulated in R94W+Veh versus Ctrl+Veh or downregulated in R94W+CNO versus R94W+Veh. Bar length indicates gene number; adjusted $P < 0.05$. (c) Heatmap showing group-averaged, row-scaled expression of immune-, inflammatory-, and serotonergic-pathway-related DEGs. (d,e) Representative images of MYD88 (d) or NF-κB p65 (e) in mCherry-positive microglia from the indicated groups. Nuclei were counterstained with DAPI (cyan). Scale bars, 10 μm. (f) Quantification of MYD88 fluorescence intensity within mCherry-positive microglia. (g) Representative Western blots and quantification of MYD88 and TLR4 in BLA lysates normalized to β-actin; total NF-κB p65 was also assessed by Western blotting. (h) Quantification of NF-κB p65 fluorescence intensity within mCherry-positive microglia. Data are mean ± SEM. For immunofluorescence, each dot represents the per-mouse mean calculated from three fields; for Western blotting, each dot represents one mouse. One-way ANOVA followed by Tukey's multiple-comparisons test. $^{**}P < 0.01$ and $^{***}P < 0.001$.

Figure 9. AMG487 treatment attenuates behavioral and CXCL10-associated neuroimmune abnormalities in Mfn2 R94W/+ mice. (a) Representative elevated-plus-maze trajectories and quantification of time spent in the open arms, time spent in the closed arms, and the proportion of open-arm duration relative to total arm duration in WT, R94W, and R94W+AMG487 mice. OA, open arms; CA, closed arms. (b) Number of marbles buried in the marble-burying test. (c) CD8α-positive cells per square millimeter in the BLA. (d) Mean CXCL10 fluorescence intensity within Iba1-positive microglial areas. (e) Representative CD8α immunofluorescence images. DAPI, blue. Enlarged images are shown. Scale bar, 10 μm. (f) Representative images of CXCL10 (red) in Iba1-positive microglia (green). DAPI, blue. Scale bar, 10 μm. Data are presented as mean ± SEM, and each dot represents one mouse. For immunofluorescence analyses, each value represents the per-mouse mean calculated from multiple fields of view. Statistical significance was assessed using one-way ANOVA followed by Tukey's multiple-comparisons test. $^{*}P < 0.05$, $^{**}P < 0.01$, and $^{***}P < 0.001$.

Supplementary figure legends

Supplementary Figure 1. Assessment of locomotor activity, anxiety-like behavior, and depressive-like behavior in WT, T105M, and R94W mice. (a) Representative open-field test (OFT) parameters, including total distance traveled, number of entries into the central area, and distance traveled in the central area. T105M mice exhibited a significant reduction in total distance traveled compared with WT mice. (b) Schematic illustration of the forced swimming test (FST) and quantification of the number of immobility episodes and total immobility time. Data are presented as mean ± SEM; each dot represents one mouse. Statistical significance was determined using one-way ANOVA followed by Tukey's multiple-comparisons test. $^{*}P < 0.05$.

Supplementary Figure 2. Histological characterization of major brain cell types and cell-type distribution of *Mfn2* expression. (a) Representative NeuN images of coronal brain sections and BLA enlargements from WT and *Mfn2*$^{R94W/+}$ mice. (b) Representative GFAP images of the BLA and hippocampus. (c) Representative Iba1 images of the BLA and hippocampus, with quantification of the Iba1-positive area in the BLA. (d) Cell-type expression profiles of *Mfn2* and *Aif1* obtained from the Allen Brain Cell Atlas using its built-in online analysis platform. (e) UMAP feature plots showing the distribution of *Mfn2* and *Aif1* expression, generated using the same online platform.

Supplementary Figure 3. Effects of microglial Gi-DREADD activation on Iba1 and GFAP expression in the BLA. (a) Western blots of Iba1 and GFAP; β-actin was the loading control. Vertical dividing lines indicate removal of intervening blank lanes; all samples were derived from the same membrane and processed identically. (b) Densitometric quantification normalized to β-actin. Data are mean ± SEM; each dot represents one mouse. One-way ANOVA followed by Tukey's test. $^{*}P < 0.05$ and $^{**}P < 0.01$.

Supplementary Figure 4. GO enrichment analysis of genes downregulated in *Mfn2* $^{R94W/+}$ mice and genes upregulated after microglial Gi-DREADD activation. (a) GO analysis of genes downregulated in R94W+Veh versus Ctrl+Veh. (b) GO analysis of genes upregulated in R94W+Gi versus R94W+Veh. Terms are classified as BP, CC, or MF; bar length indicates gene number. Adjusted $P < 0.05$.

Supplementary Figure 5. Evaluation of synaptic and mitochondrial alterations in the BLA of *Mfn2* $^{R94W/+}$ mice.
(a) Representative Western blots and quantification of synaptophysin (SYP) in BLA lysates from the Ctrl+Veh, R94W+Veh, and R94W+CNO groups. (b) Gene counts assigned to selected synapse-related GO cellular-component terms; none showed significant enrichment after multiple-testing correction. (c) Heatmap showing row-scaled expression of mitochondrial function-related DEGs between Ctrl+Veh and R94W+Veh mice. (d) Representative Western blots and quantification of COX IV in BLA lysates. β-actin was used as the loading control. (e) Representative images of COX IV (yellow) and mCherry-positive microglia (red) in the indicated groups. Nuclei were counterstained with DAPI (blue). Scale bars, 10 μm. Data are mean ± SEM; each dot represents one mouse. One-way ANOVA followed by Tukey's multiple-comparisons test. $^{**}P < 0.01$ and $^{***}P < 0.001$.

Supplementary Figure 6. Immune-inflammatory and serotonergic pathway-related transcriptional changes following microglial Gi-DREADD activation. (a) Row-scaled expression of all identified DEGs associated with enriched innate immune, inflammatory, and serotonergic pathways. (b) Normalized transcript abundance of *C3*, *Il1a*, *Nlrp3*, *Htr2c*, *Casp1*, and *Tlr7*. Data are mean ± SEM; each dot represents one mouse. (c,d) Representative three-dimensional renderings of MYD88 or NF-κB p65 in mCherry-positive microglia, shown from two viewing angles. Scale bar, 5 μm. (e) Representative NLRP3 images in mCherry-positive microglia. DAPI, blue. Scale bar, 20 μm.

Supplementary Figure 7. Effects of AMG487 treatment on microglia-associated synaptic material in the BLA of *Mfn2* $^{R94W/+}$ mice. (a) Representative images of SYP (red), Iba1 (green), and DAPI (blue) in control, R94W, and AMG487-treated R94W mice. (b) Corresponding images of PSD95 (magenta), Iba1 (green), and DAPI (blue). The representative images show reduced spatial overlap of SYP- or PSD95-positive puncta with Iba1-positive microglia after AMG487 treatment; these observations were not quantified.

Supplementary Figure 8. TRP-channel expression and assessment of TRPV4 in LPS-stimulated BV2 cells and the BLA.
(a) PCA of BLA RNA-sequencing samples from the Ctrl, R94W, and R94W+Gi groups. (b) Heatmap showing row-scaled expression of selected TRP-channel and mechanosensitive ion-channel genes. (c) Representative Western blot of TRPV4 in BV2 cells exposed to increasing concentrations of LPS. (d,e) Representative Western blot and quantification of TRPV4 in independent BV2 samples treated with 1 μg/mL LPS. β-actin was used as the loading control. (f,g) Quantification and representative images of TRPV4 immunoreactivity in the BLA of Ctrl+Veh, R94W+Veh, and R94W+CNO mice. TRPV4 showed minimal spatial overlap with mCherry-positive microglia. Nuclei were counterstained with DAPI (blue). Scale bar, 20 μm. Data are mean ± SEM. $^{**}P < 0.01$ and $^{***}P < 0.001$.

Supplementary Figure 9. GSEA of public human CMT2A fibroblast transcriptomic data. Gene set enrichment analysis was performed using the publicly available GSE158650 RNA-seq dataset, comparing fibroblast lines carrying the *MFN2* R274W or H361Y variant (CMT2A, $n = 2$) with healthy control fibroblast lines ($n = 3$). Enrichment plots are shown for interferon-γ response, TNF-α signaling via NF-κB, inflammatory response, antigen processing and presentation, Toll-like receptor signaling, phagosome, complement, and oxidative phosphorylation. Positive normalized enrichment scores (NESs) indicate enrichment toward genes more highly expressed in CMT2A fibroblasts, whereas negative NESs indicate enrichment toward genes more highly expressed in control fibroblasts. NES, nominal P values, and false discovery rate (FDR) q values are indicated in each plot.

Supplementary Video 1. Three-dimensional rotational rendering of PSD95-positive puncta within an mCherry-positive BLA microglial volume from an R94W+Veh mouse. Red, mCherry; cyan, PSD95; blue, DAPI.

Supplementary Video 2. Three-dimensional rotational rendering of PSD95-positive puncta within an mCherry-positive BLA microglial volume from an R94W+CNO mouse following Gi-DREADD activation. Red, mCherry; cyan, PSD95; blue, DAPI.

Tab.1

Antibody list

Antibody	Species/Clonality	Source (Catalogue no,)	Dilution	Usage
Anti-NLRP3	Rabbit/monoclonal	Beyotime/AF2155	1:200	IF
Anti-GFAP	Rabbit/polyclonal	Abcam/ab7260	1:1000/1:200	WB/IF
Anti-NF-κB p65	Rabbit/monoclonal	Abcam/ab32536	1:1000/1:200	WB/IF
Anti-Iba1	Mouse/monoclonal	Proteintech/66827-1-Ig	1:1000/1:200	WB/IF
Anti-CD8α	Rabbit/polyclonal	wanleibio/W01071102	1:200	IF
Anti-COX IV	Mouse/monoclonal	Abcam/Abcam33985	1:200	IF
Anti-COX IV	Rabbit/polyclonal	Proteintech/11242-1-AP	1:1000	WB
Anti-NeuN	Rabbit/monoclonal	Abcam/ab177487	1:200	IF
Anti-SYP	Rabbit/polyclonal	Beyotime/AF8091	1:1000/1:200	WB/IF
Anti-PSD95	Rabbit/polyclonal	Abcam/ab18258	1:200	IF
Anti-CXCL10	Rabbit/monoclonal	Abcam/ab137018	1:200	IF
Anti-TLR4	Rabbit/monoclonal	Abcam/ab13556	1:1000	WB
Anti-MYD88	Rabbit/polyclonal	Beyotime/AF7524	1:1000/1:200	WB/IF
Anti-TRPV4	Rabbit/polyclonal	Beyotime/AF8253	1:1000/1:200	WB/IF
Anti-Total OXPHOS	Mouse/monoclonal	Abcam/ab110413	1:2000	WB
Anti-β-actin	Mouse/monoclonal	UTIBODY/UM4006	1:2000	WB
Anti-GAPDH	Mouse/monoclonal	UTIBODY/UM4002	1:2000	WB
Anti-Rabbit IgG (H+L)	Goat/polyclonal	SeraCare/5220-0336	1:5000	WB
Anti-Mouse IgG (H+L)	Goat/polyclonal	SeraCare/5220-0341	1:5000	WB
Alexa Fluor 488-conjugated anti-rabbit IgG	Goat	Abcam/ab150077	1:1000	IF
Alexa Fluor 647-conjugated anti-rabbit IgG	Goat	Invitrogen/A32728	1:1000	IF
Alexa Fluor 594-conjugated anti-rabbit IgG	Goat	Abcam/ab150080	1:1000	IF
Alexa Fluor 488-conjugated anti-mouse IgG	Goat	Invitrogen/A11029	1:1000	IF
Alexa Fluor 647-conjugated anti-mouse IgG	Goat	Invitrogen/A21236	1:1000	IF

Figure.1

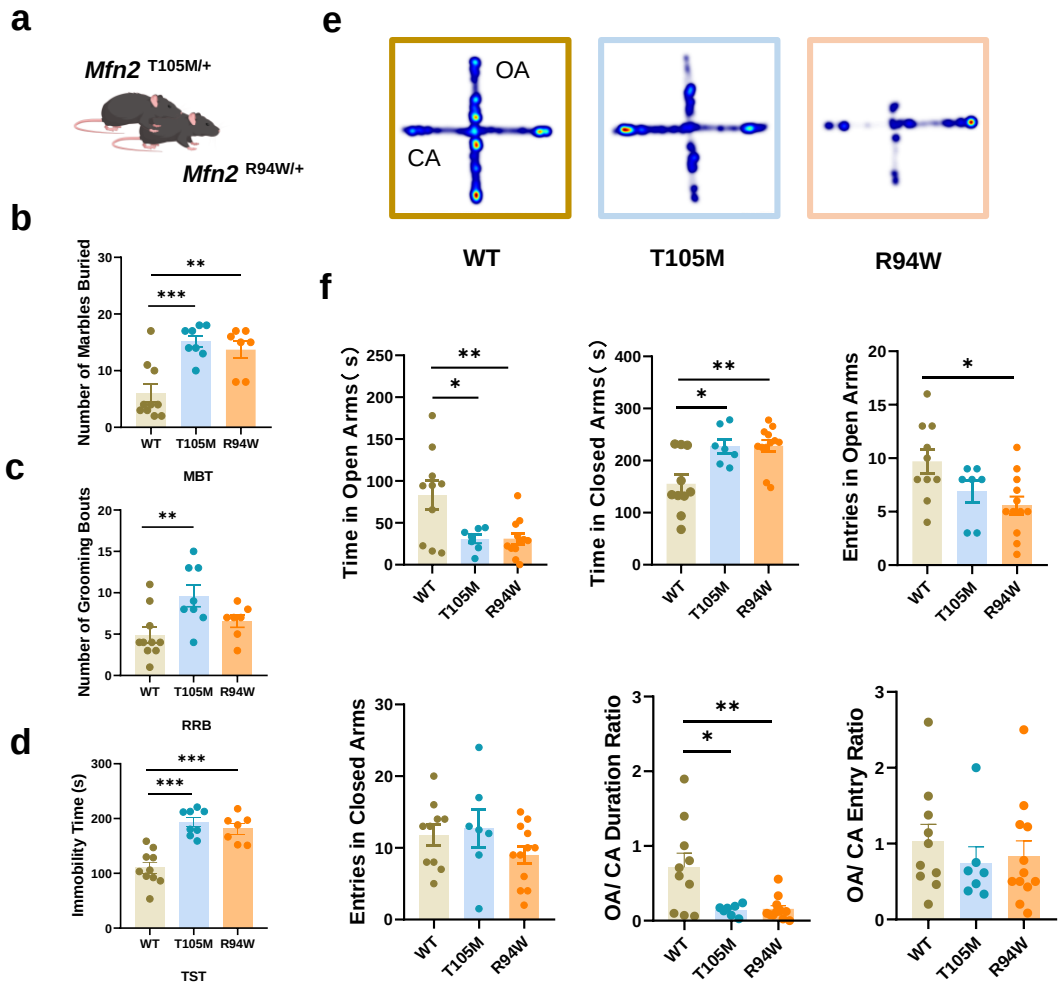

Figure.2

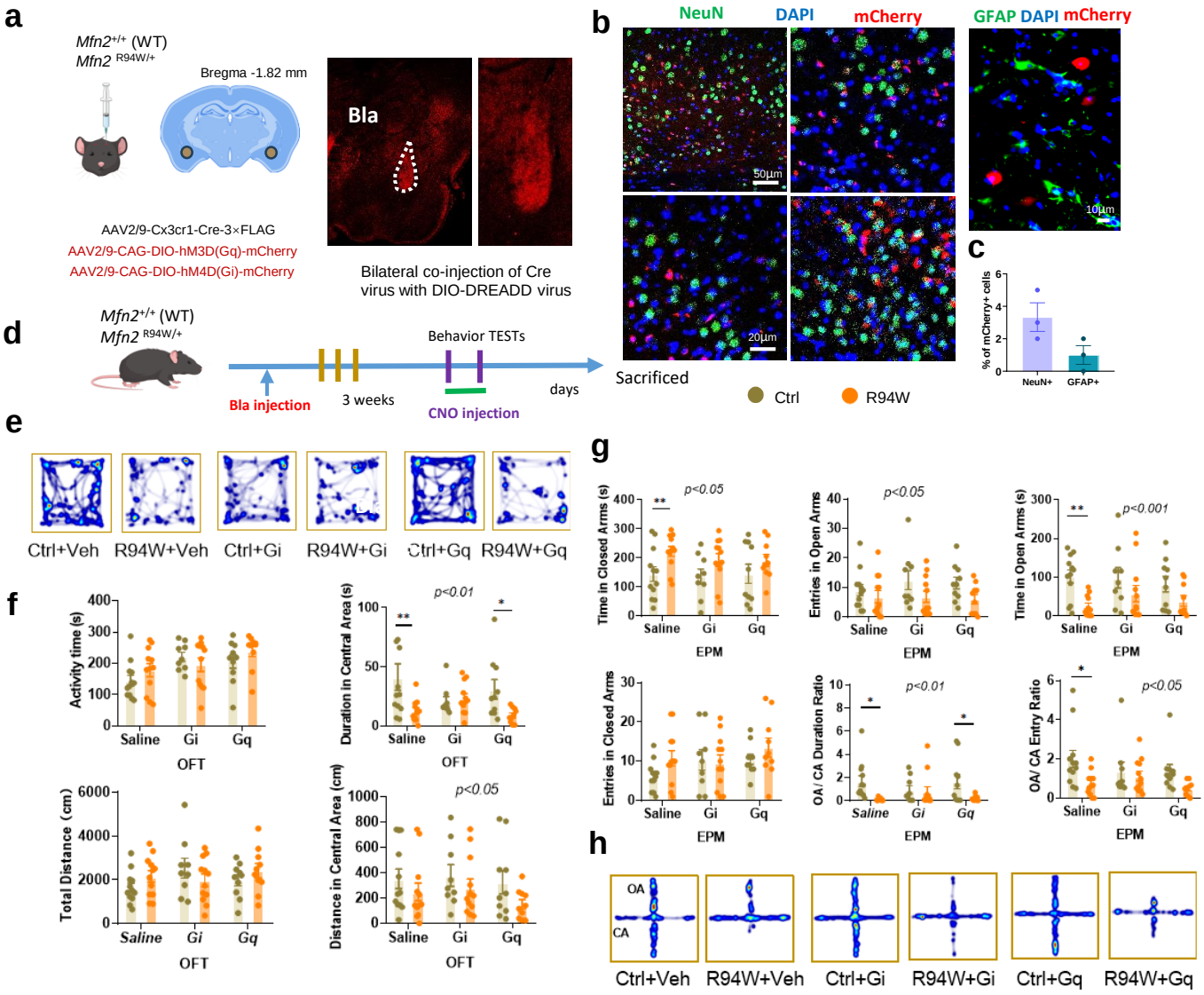

Figure.3

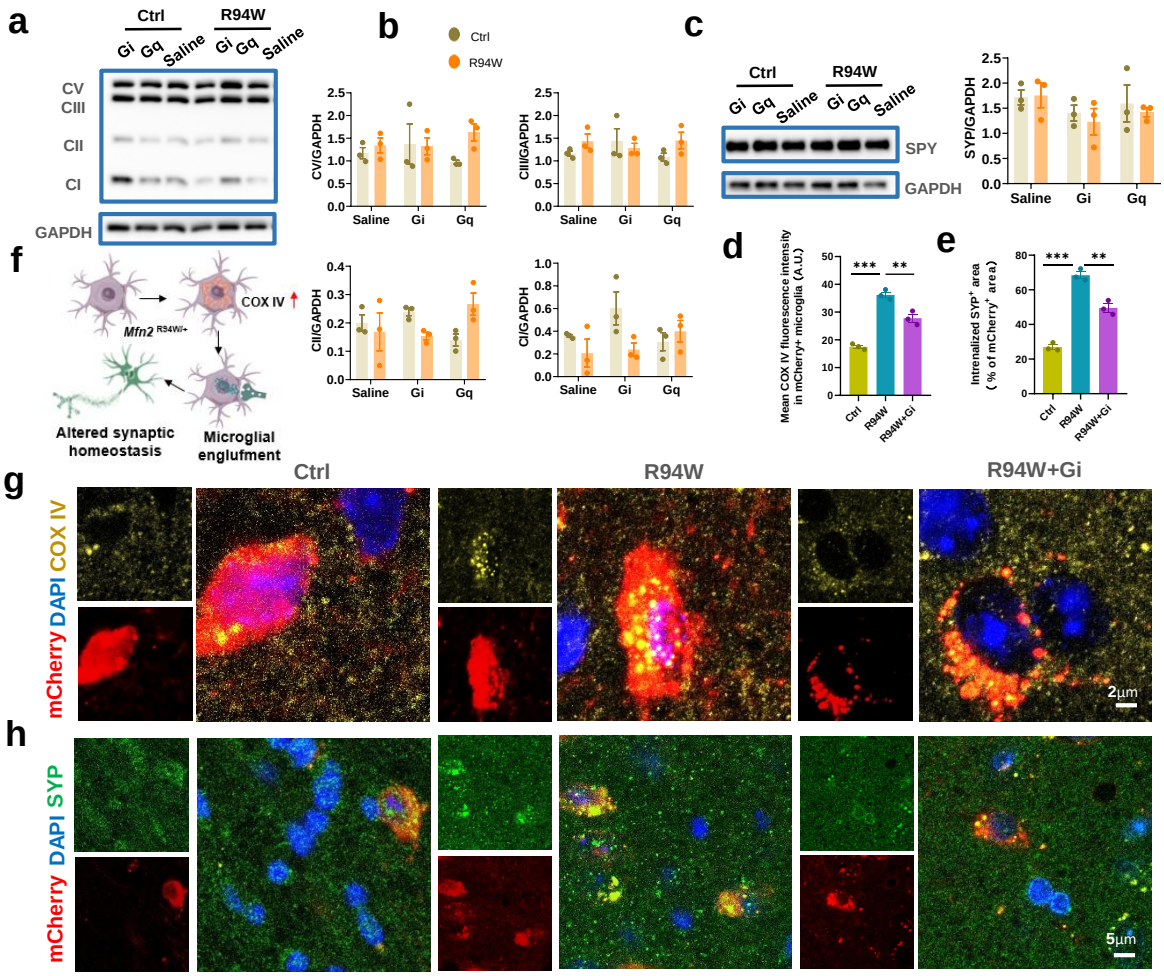

Figure.4

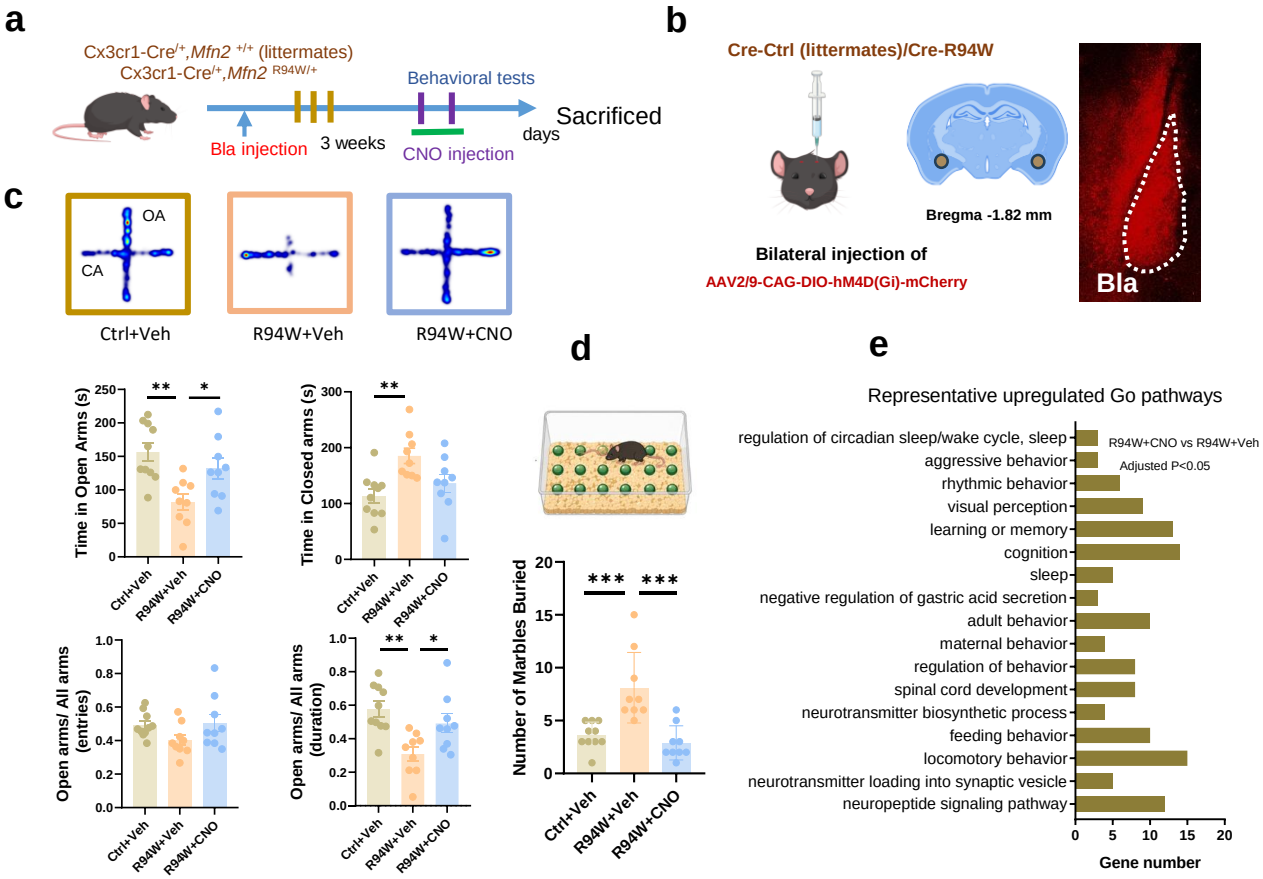

Figure.5

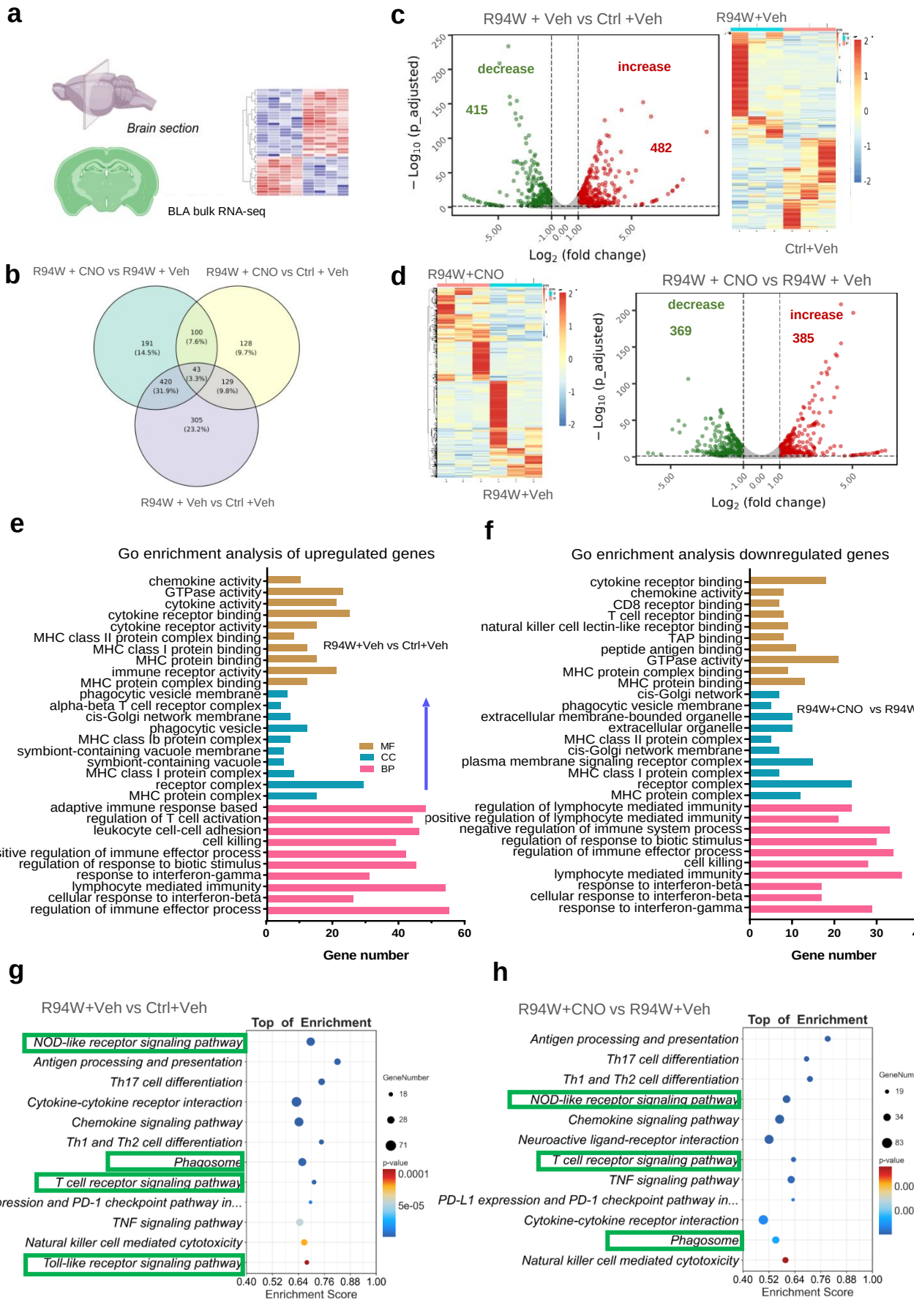

Figure.6

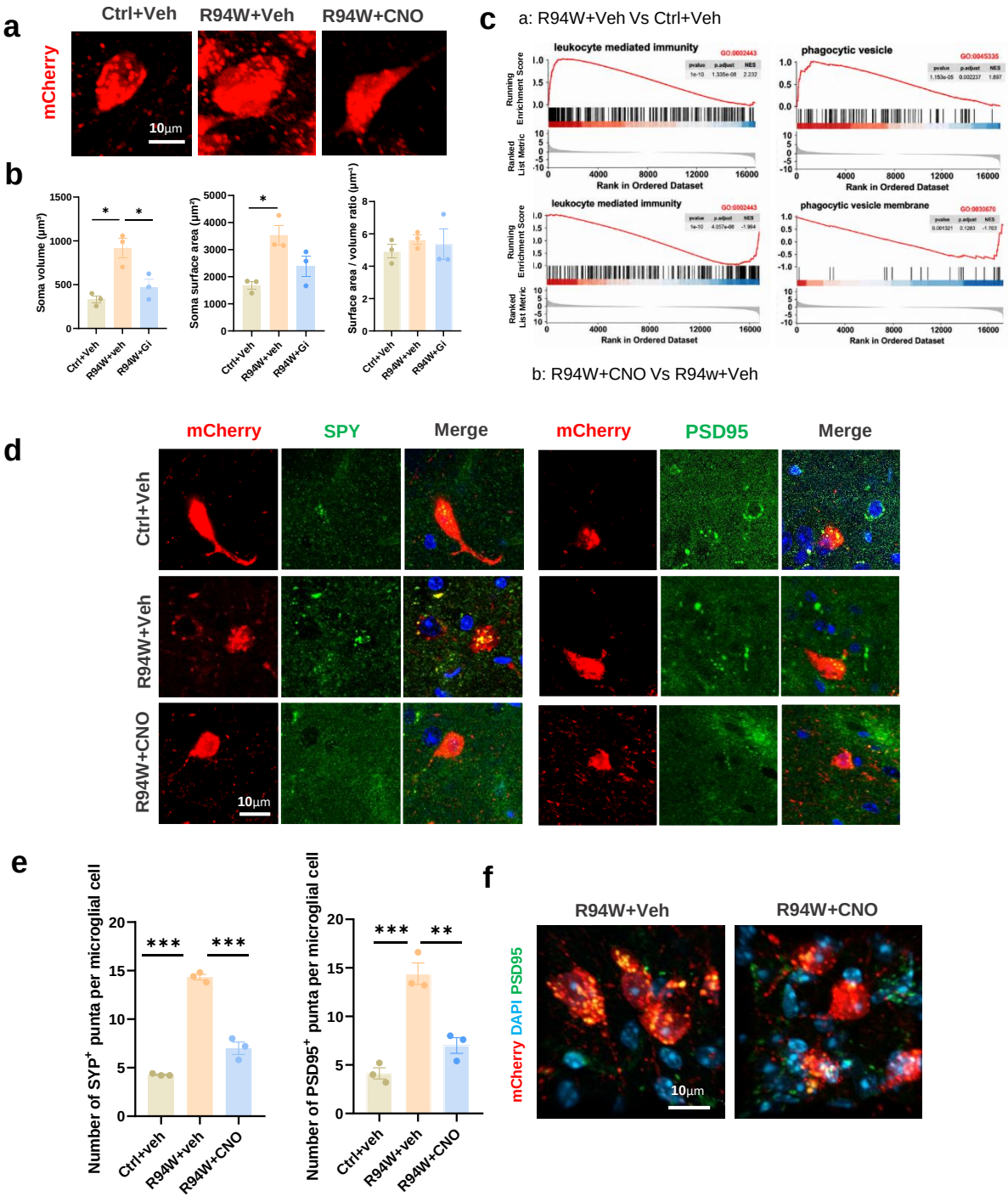

Figure.7

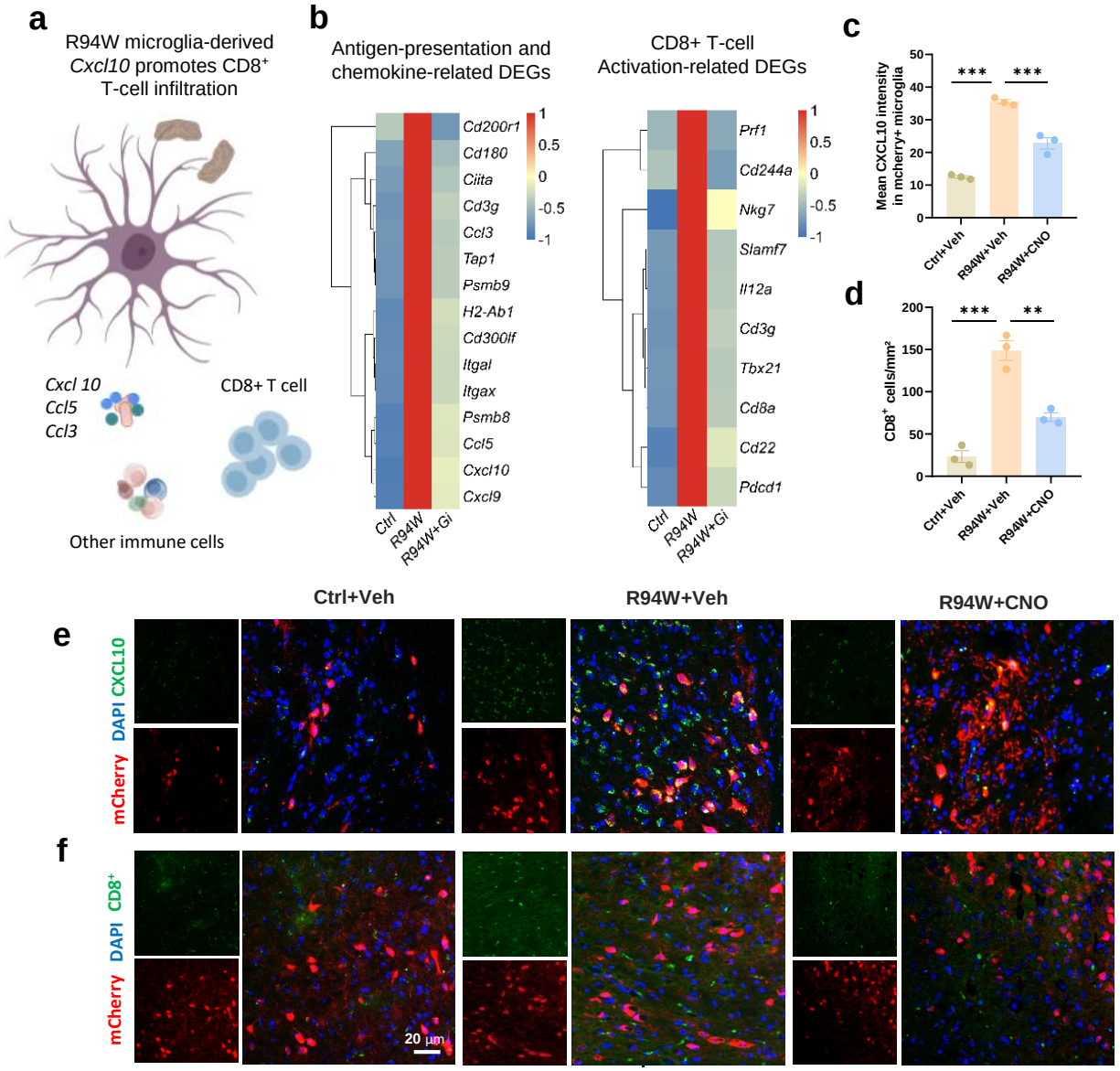

Figure.8

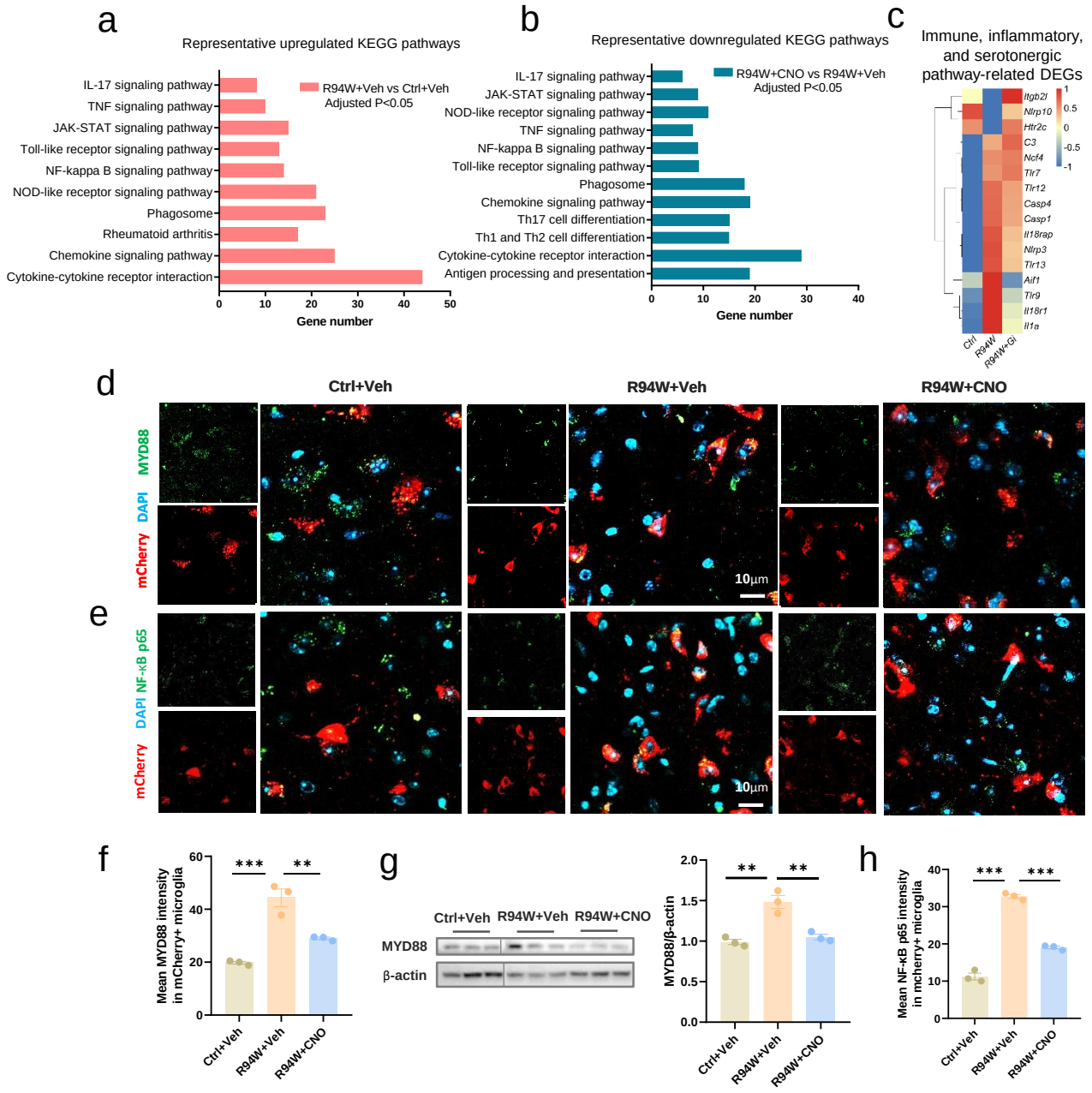

Figure.9

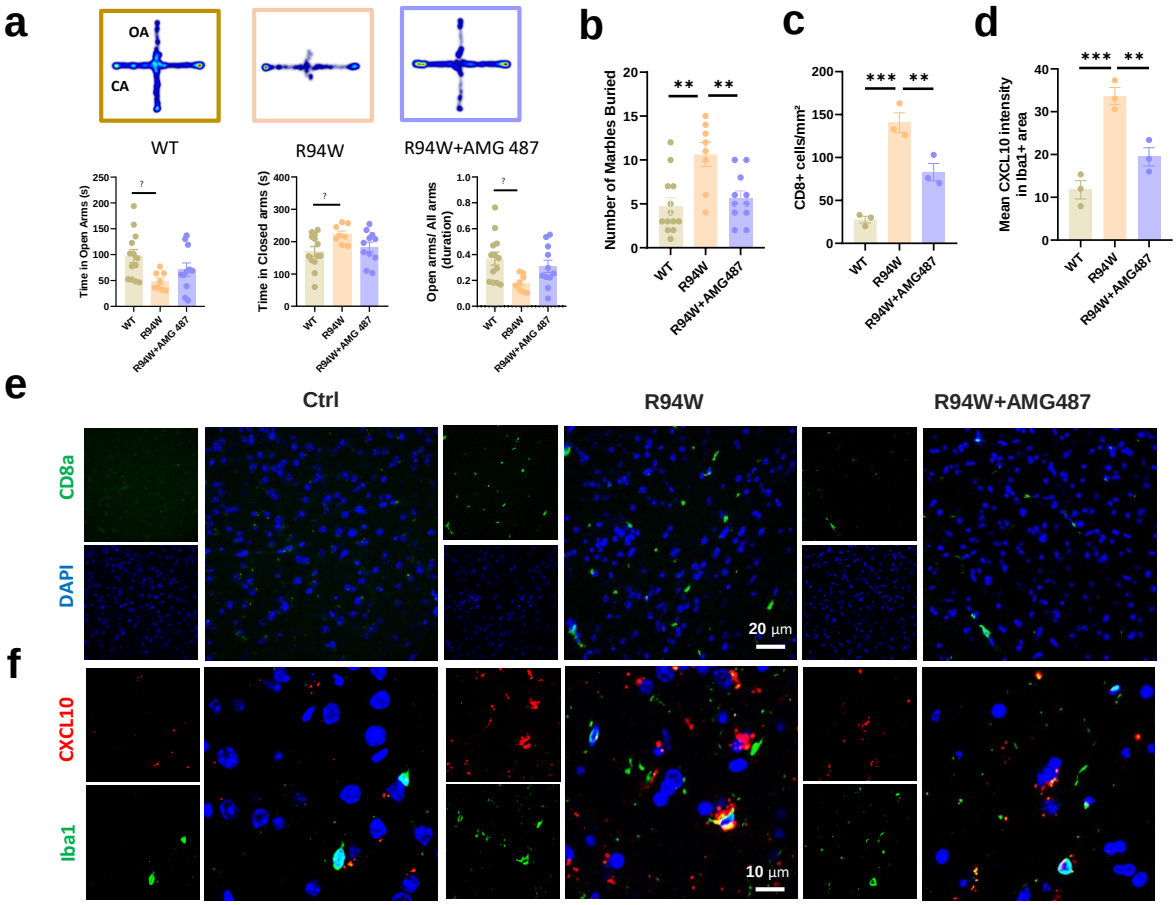

Supplementary Figure 1

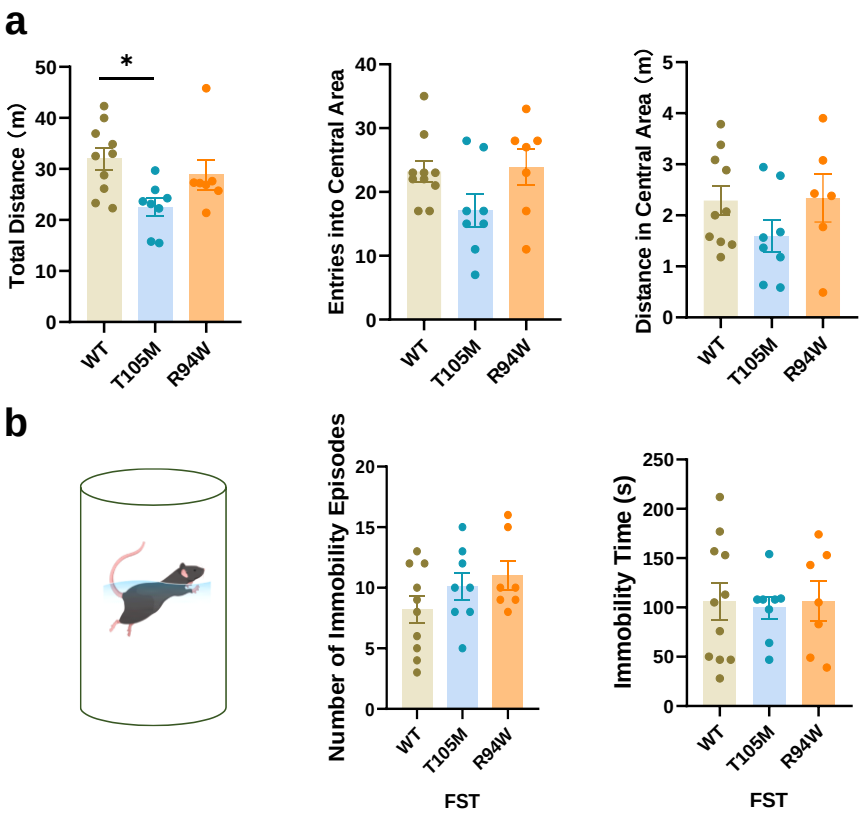

Supplementary Figure 2

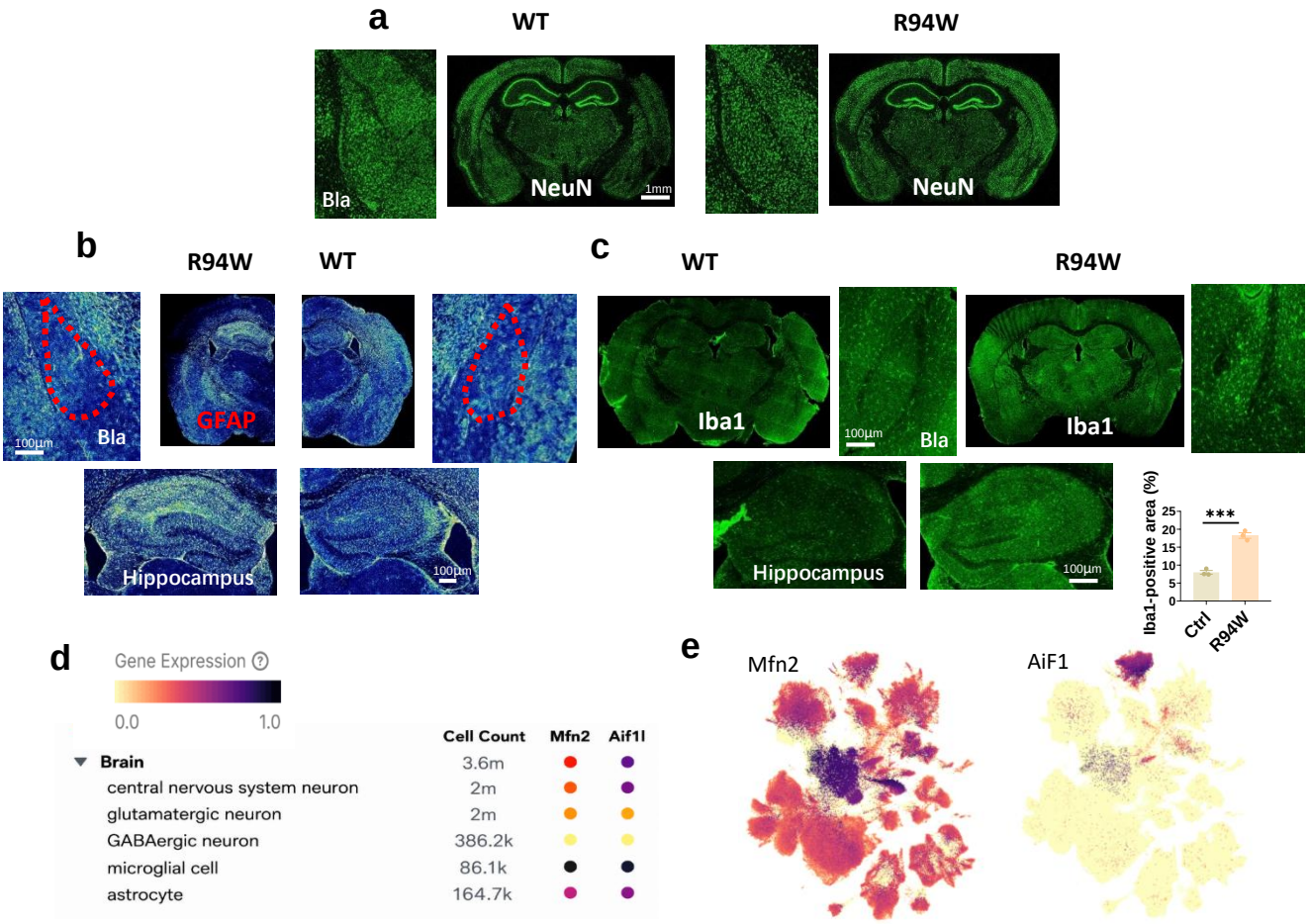

Supplementary Figure 3

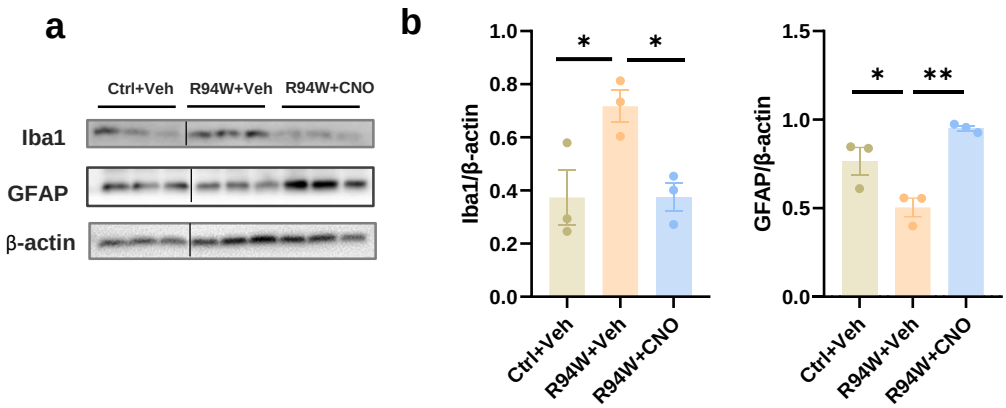

Supplementary Figure 4

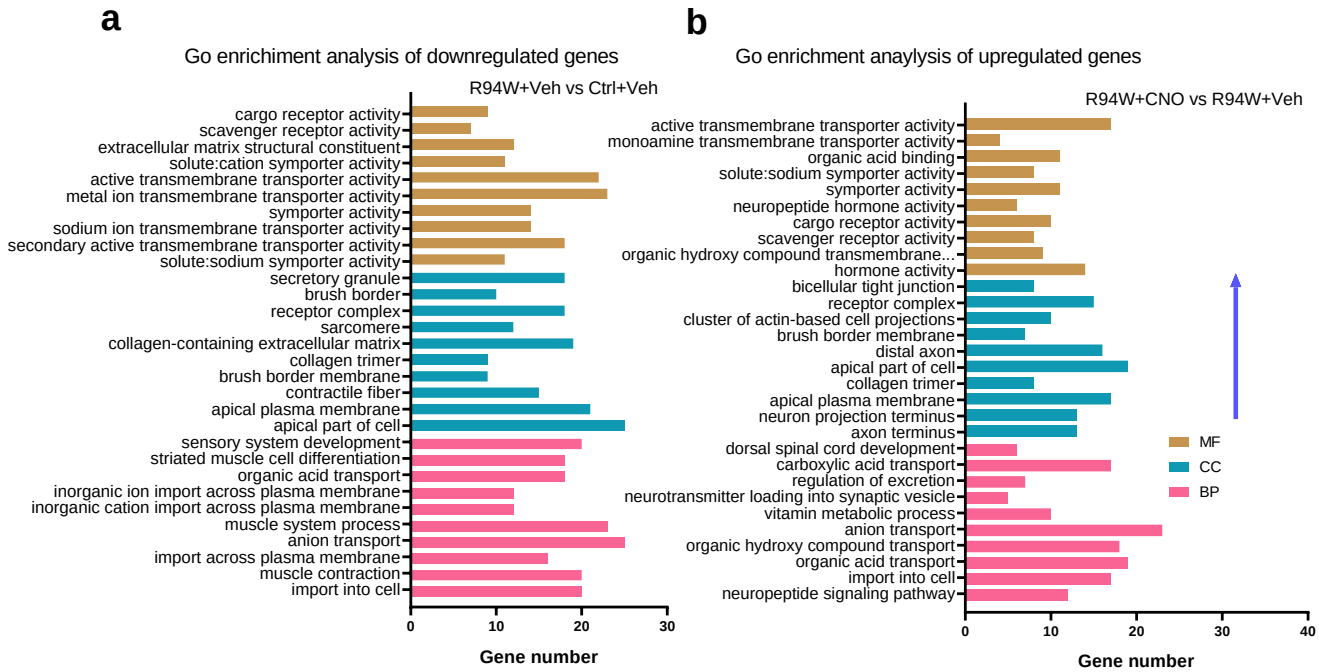

Supplementary Figure 5

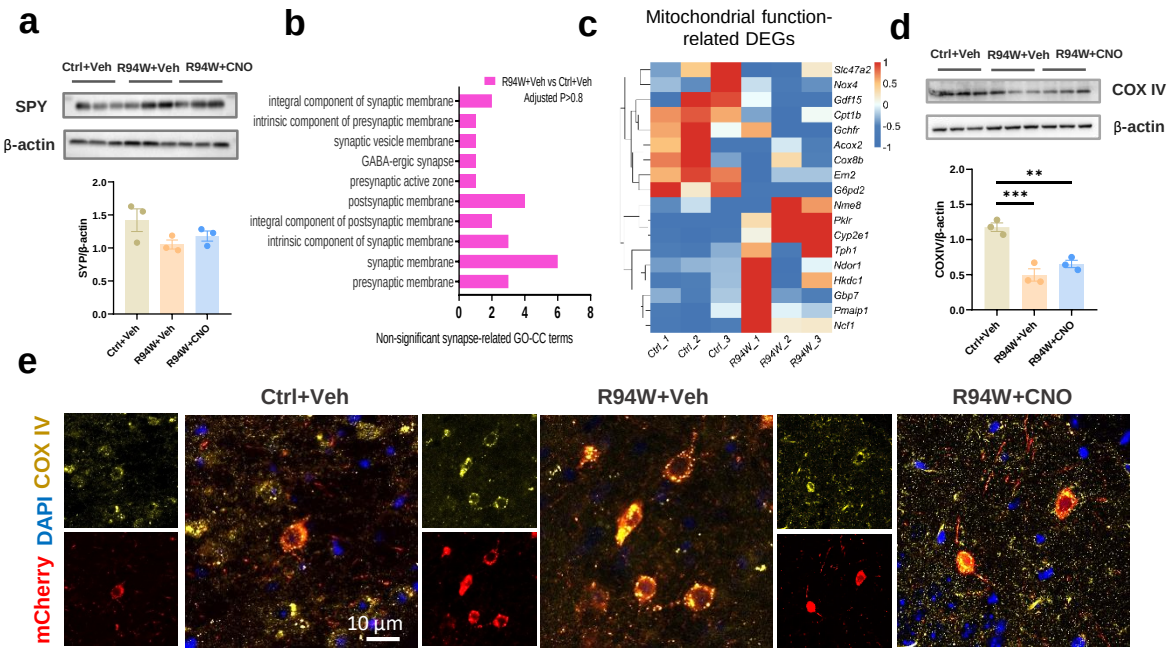

Supplementary Figure 6

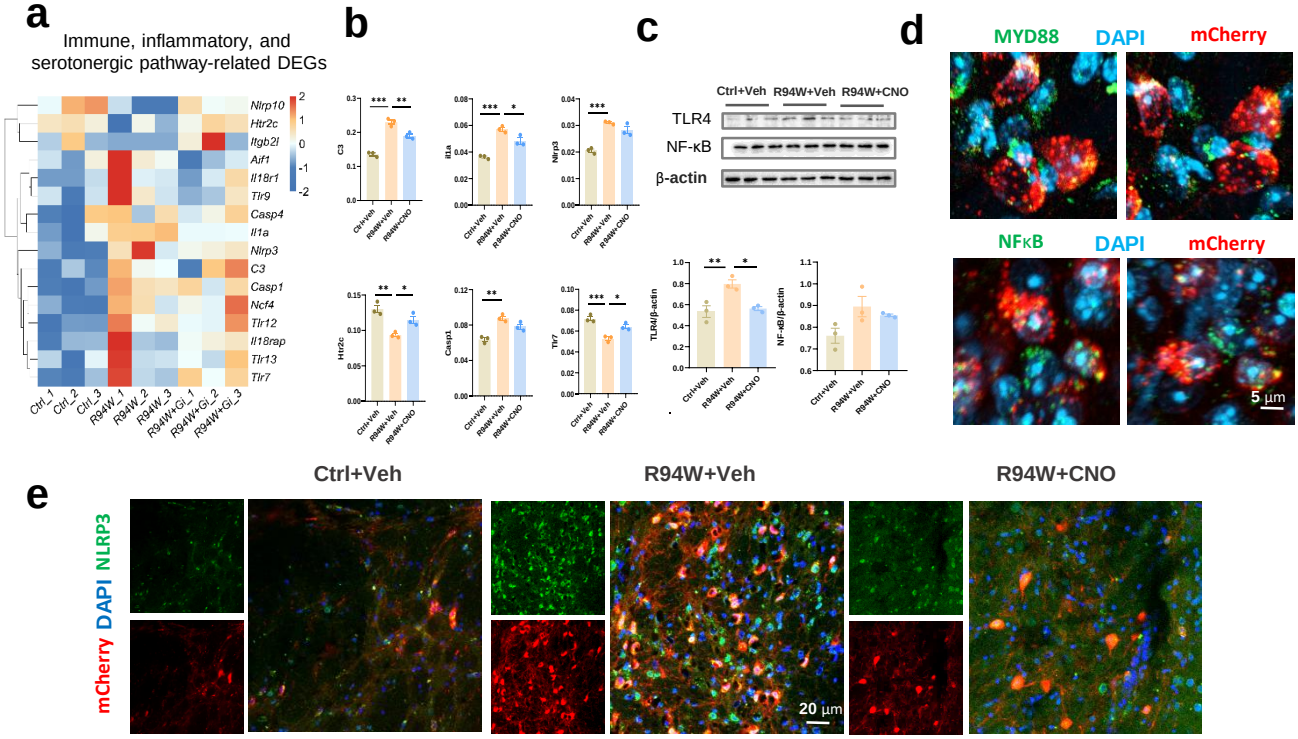

Supplementary Figure 7

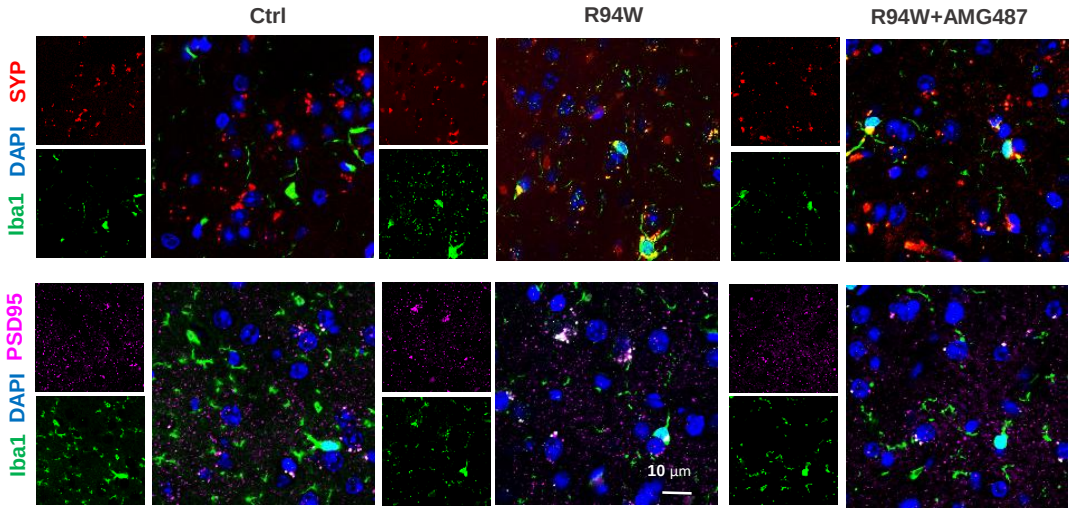

Supplementary Figure 8

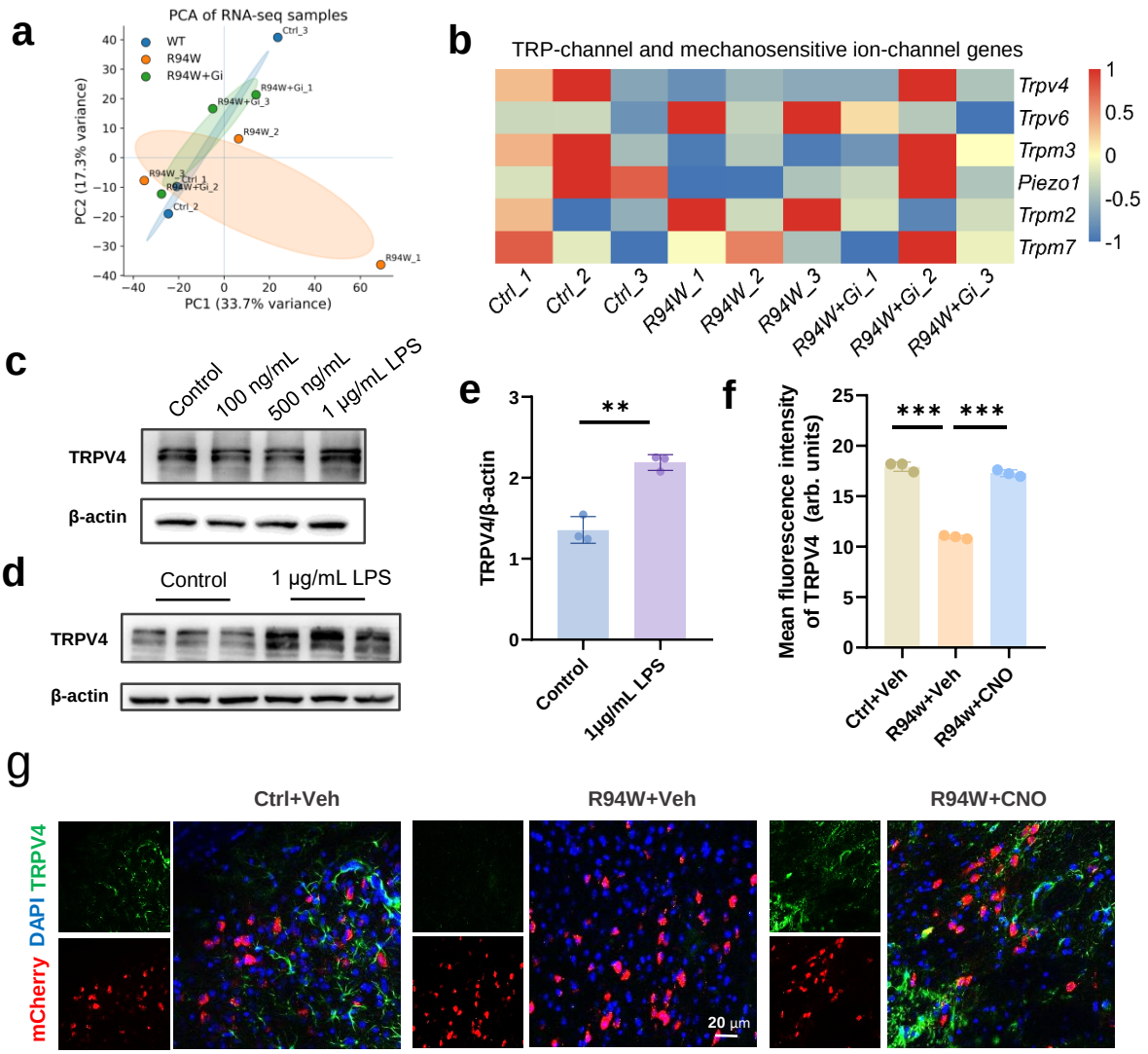

Supplementary Figure 9

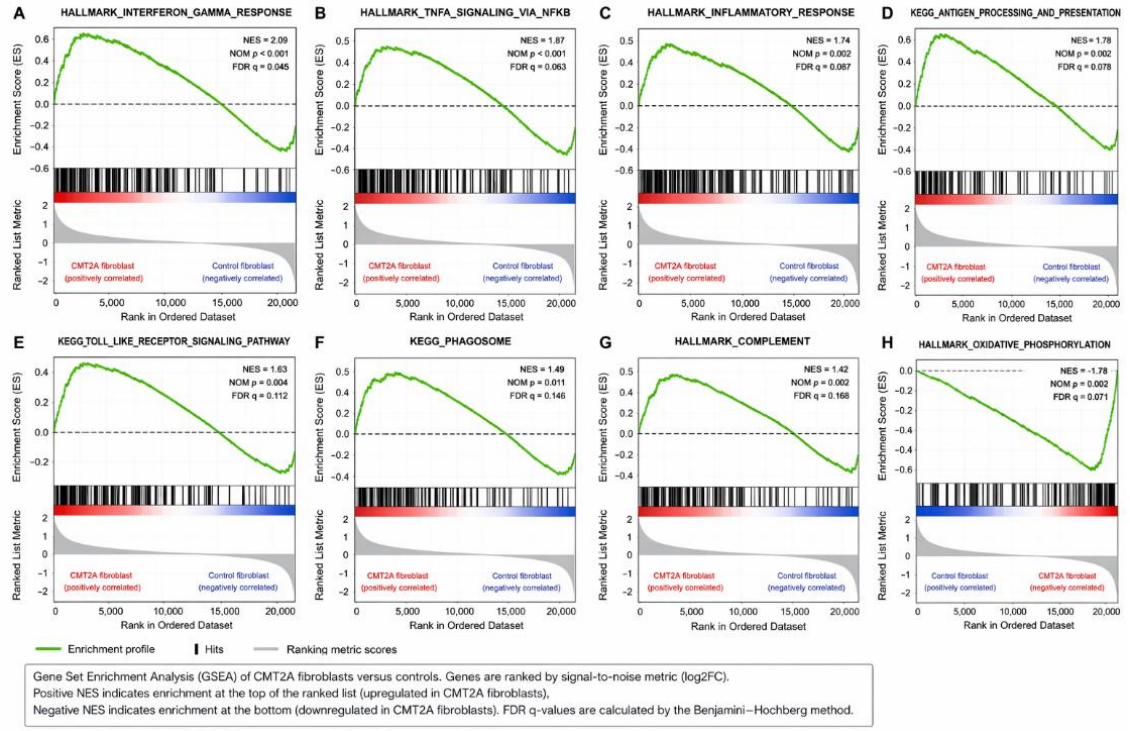

Gene Set Enrichment Analysis (GSEA) of CMT2A fibroblasts versus controls. Genes are ranked by signal-to-noise metric (log2FC).
Positive NES indicates enrichment at the top of the ranked list (upregulated in CMT2A fibroblasts),
Negative NES indicates enrichment at the bottom (downregulated in CMT2A fibroblasts). FDR q-values are calculated by the Benjamini–Hochberg method.

Supplementary Video 1.

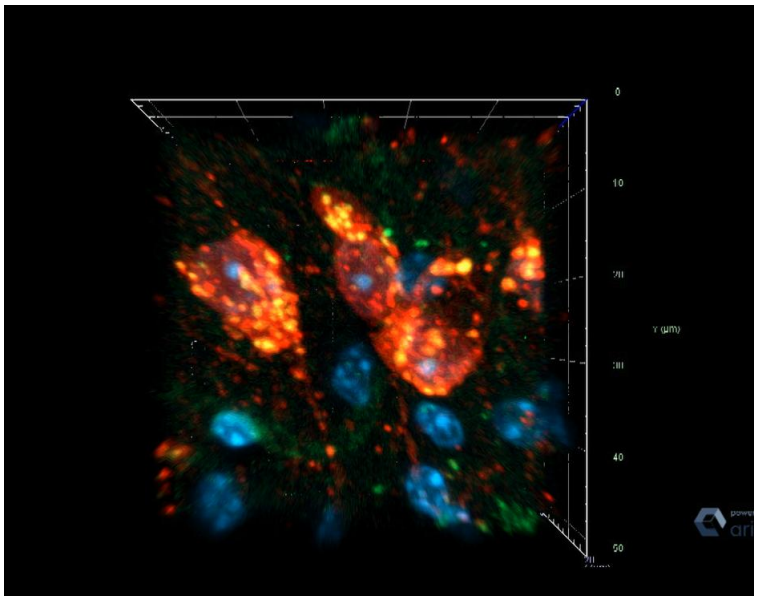

Supplementary Video 2.

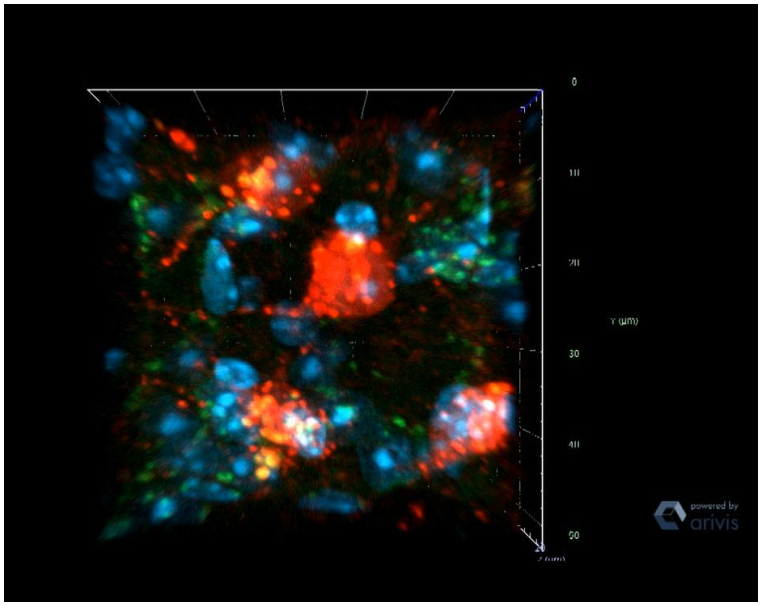

Graphical Abstract

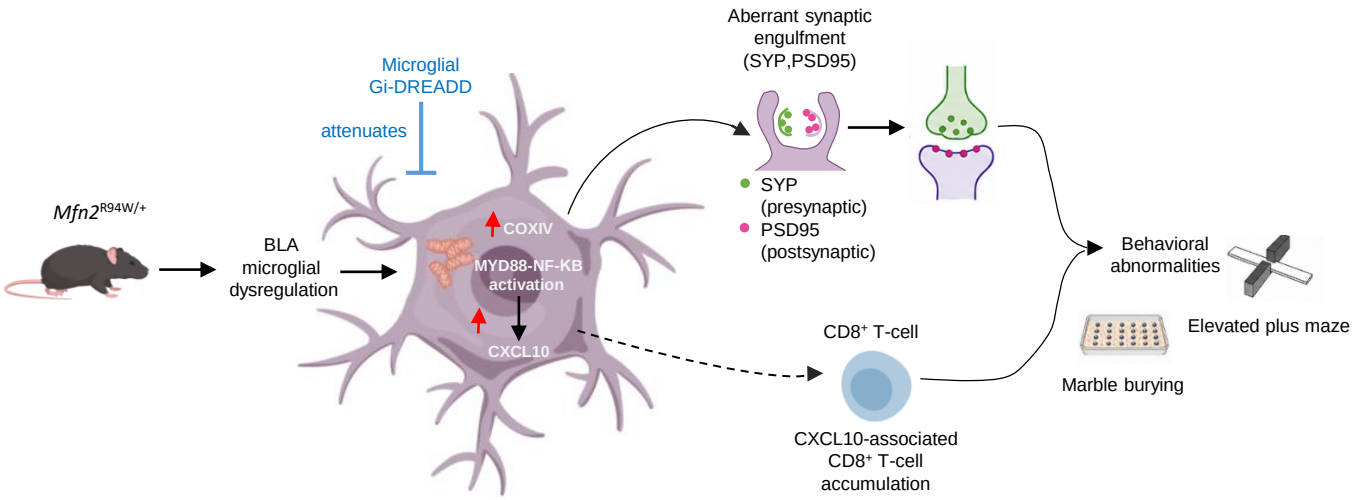

Supplementary Data 1. Uncropped Western blot images corresponding to the main and supplementary figures.

immunoblots for OXPHOS and GAPDH corresponding to Fig. 3a

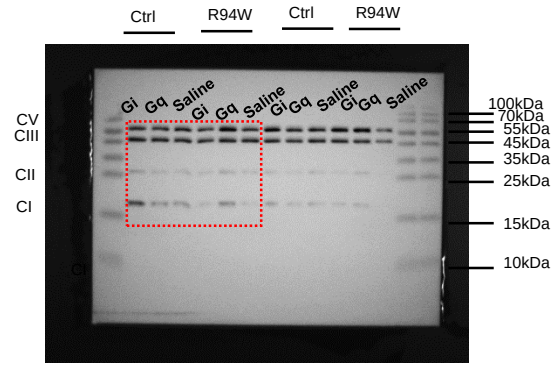

Red boxes indicate the regions cropped and presented in the corresponding figures.

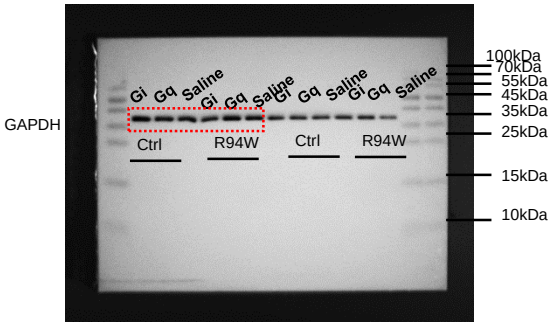

immunoblots for SYP and GAPDH corresponding to Fig. 3c

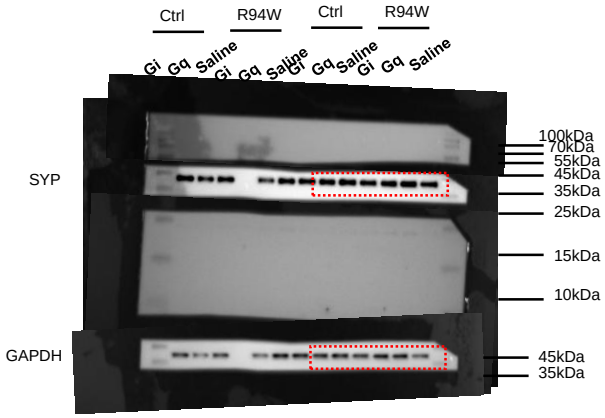

immunoblots for MYD88 and β-actin corresponding to Fig. 8f

immunoblots for iba1 corresponding to Supplementary. Fig.3a

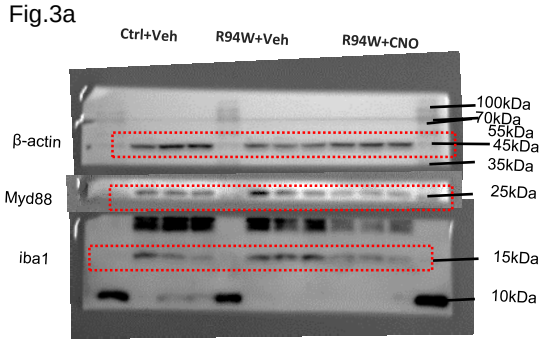

Immunoblots for GFAP and β-actin corresponding to Supplementary. Fig.3a (Uncropped membrane strips)

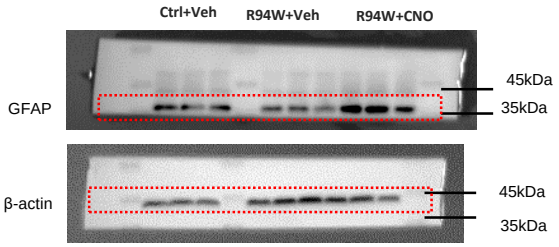

Immunoblots for SYP and β-actin corresponding to Supplementary. Fig.5a (Uncropped membrane strips)

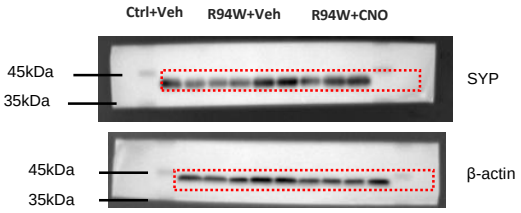

Immunoblots for COX IV and β-actin corresponding to Supplementary Figure.5d

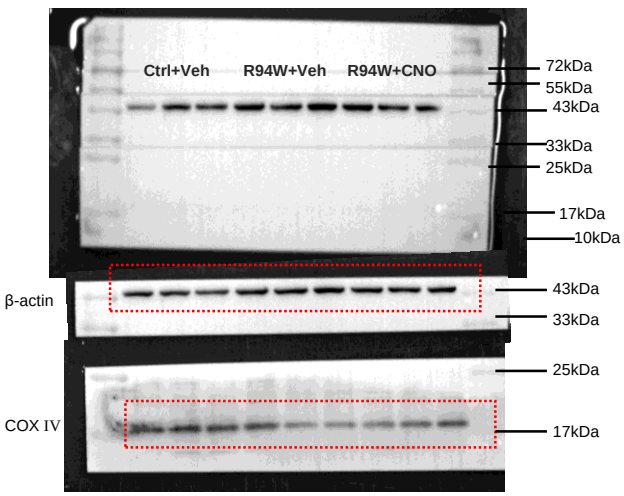

Immunoblots for TLR4, NF-Kb and β-actin corresponding to Supplementary Fig.6c

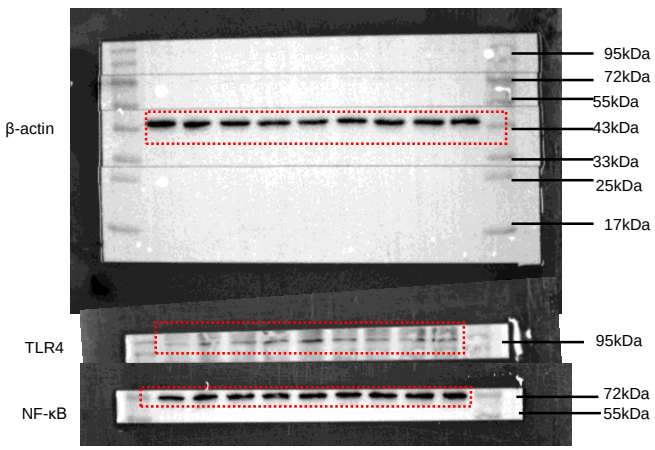

Uncropped immunoblots for TRPV4 and β-actin corresponding to Supplementary Fig. 7c

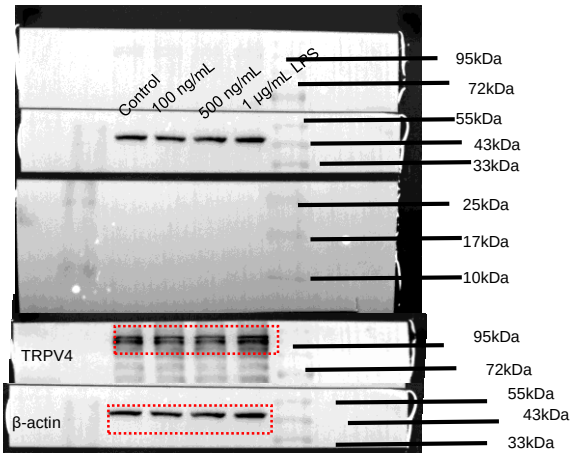

Immunoblots for TRPV4 and β-actin corresponding to Supplementary Fig.7d